Building a Low-Cost Portable VO2 Max Mask

BY

SHASHWAT SINHA
B.S., University of Illinois at Chicago, 2024

THESIS

Submitted as partial fulfillment of the requirements
for the degree of Master of Science in Electrical and Computer Engineering
in the Graduate College of the
University of Illinois at Chicago, 2026

Chicago, Illinois

Defense Committee:

Dieff Vital, Chair and Advisor
Jarrad Hampton-Marcell, Co-Advisor
Mesrob Ohanessian, Electrical and Computer Engineering
Benjamin Sanchez Terrones, Electrical and Computer Engineering

To my parents, Abhimanyu and Babita Sinha, whose unwavering support and belief in me made all of this possible and to my brother, Saransh Sinha, who carved a path for me to follow.

ACKNOWLEDGMENTS

I would like to thank my thesis committee—Dr. Dieff Vital, Dr. Jarrad Hampton-Marcell, Dr. Mesrob Ohanessian, and Dr. Benjamin Sanchez Terrones—for their guidance and support throughout this research. I am grateful to Dr. Vital for appointing me as his graduate research assistant, which made this work possible. I am equally grateful to Dr. Hampton-Marcell for providing access to his laboratory and equipment, which were essential for building and testing the prototype.

I also wish to acknowledge the Department of Electrical and Computer Engineering at the University of Illinois at Chicago for providing the resources necessary to complete this work.

Finally, I would like to thank my family and friends for their constant encouragement and support throughout my graduate studies.

SS

TABLE OF CONTENTS

LIST OF TABLES

LIST OF FIGURES

LIST OF ABBREVIATIONS

ADC	Analog-to-Digital Converter
BLE	Bluetooth Low Energy
BPM	Breaths Per Minute
CAD	Computer-Aided Design
C_d	Discharge Coefficient
CO_2	Carbon Dioxide
COPD	Chronic Obstructive Pulmonary Disease
CPAP	Continuous Positive Airway Pressure
CSV	Comma-Separated Values
ESP32	Espressif Systems 32-bit Microcontroller
FDM	Fused Deposition Modeling
$FeCO_2$	Fraction of Expired Carbon Dioxide
FeO_2	Fraction of Expired Oxygen
$FiCO_2$	Fraction of Inspired Carbon Dioxide
FiO_2	Fraction of Inspired Oxygen
GPIO	General Purpose Input/Output
I^2C	Inter-Integrated Circuit
IRB	Institutional Review Board
ISO	International Organization for Standardization
JST-XH	JST Manufacturing Connector Series
mAh	Milliamp-Hour
MEMS	Microelectromechanical Systems
NDIR	Nondispersive Infrared
N_2	Nitrogen
O_2	Oxygen
Pa	Pascal
PCB	Printed Circuit Board
PETG	Polyethylene Terephthalate Glycol
PLA	Polylactic Acid

ppm	Parts Per Million
RER	Respiratory Exchange Ratio
SDA	Serial Data Line
SCL	Serial Clock Line
SI	Système International (International System of Units)
T_{90}	Response Time to 90% of Final Value
TFT	Thin-Film Transistor
UART	Universal Asynchronous Receiver-Transmitter
USB	Universal Serial Bus
VE	Expired Minute Ventilation
VI	Inspired Minute Ventilation
VO_2	Volume of Oxygen Consumed
VO_2 max	Maximal Oxygen Consumption
VCO_2	Volume of Carbon Dioxide Produced

SUMMARY

This thesis presents the design, implementation, and instrument-level validation of a low-cost, portable system for measuring maximal oxygen consumption (VO_2 max). The system consists of a custom 3D-printed Venturi tube for airflow measurement, three environmental sensors (differential pressure, oxygen concentration, and carbon dioxide concentration), an ESP32 microcontroller with Bluetooth Low Energy (BLE) data transmission, and a Python-based data logging and analysis pipeline.

The hardware was designed around commercially available, low-cost sensors: a Sensirion SDP810-500Pa differential pressure sensor for flow measurement through the Venturi tube, a DFRobot Gravity electrochemical oxygen sensor, and a Sensirion SCD30 nondispersive infrared carbon dioxide sensor. A dual-rate BLE transmission protocol was implemented to accommodate the different sampling rates of the pressure sensor (10 Hz) and gas sensors (0.5 Hz).

Since Institutional Review Board (IRB) approval, at the time of writing, was still in progress, all validation was limited to instrument-level characterization without human subjects. Each sensor was verified independently: the carbon dioxide sensor was tested through controlled elevation and recovery cycles using a sealed chamber with a baking soda and vinegar reaction, the oxygen sensor was verified through displacement and recovery tests using the same reaction to displace ambient oxygen, and the differential pressure sensor was characterized for zero-flow stability and airflow response through the Venturi tube. System integration testing verified the complete data pipeline from sensor acquisition through wireless transmission to data logging. A reference flow standard was not available, so the Venturi discharge coefficient was not empirically determined; a literature-based estimate is used for flow rate calculations.

The results demonstrate that the individual sensors perform within their manufacturer specifications and that the integrated system reliably captures synchronized multi-sensor data. This work establishes a characterized hardware and software platform ready for future calibration with a reference flow standard and human subject testing pending IRB approval.

CHAPTER I.
INTRODUCTION

A. Background

Maximal oxygen consumption, commonly denoted VO_2 max, is defined as the highest rate at which the body can take up, transport, and utilize oxygen during exhaustive exercise [10]. First introduced by Hill and Lupton in 1923 [10, 11], VO_2 max has widely been regarded as the gold standard indicator of cardiorespiratory fitness and aerobic capacity [10]. It also serves as a key metric for integrated functions of the pulmonary, cardiovascular, and musculoskeletal systems, reflecting the upper limit of the body's aerobic endurance capabilities [12].

The clinical significance of VO_2 max has been well researched. A study by Kodama et al. found that low cardiorespiratory fitness, as measured by VO_2 max, can be a better predictor of all-cause mortality than traditional health risk factors such as hypertension, smoking, and diabetes [13]. Their findings suggest that a single metabolic equivalent (3.5 mL/kg/min) increase in aerobic capacity comes with a 13% reduction in all-cause mortality and a 15% decrease in cardiovascular mortality. Mandsager et al. reinforced these findings in a large retrospective study of 122,007 patients who underwent exercise treadmill testing over a 23-year period at Cleveland Clinic. Their results showed that low cardiorespiratory fitness carried a mortality risk comparable to or greater than smoking and diabetes, and that individuals in the highest fitness category had an 80% lower all-cause mortality compared to those in the lowest category, with no observed upper limit of benefit from increased fitness [14]. These findings contributed to the American Heart Association recommending that cardiorespiratory fitness be assessed as a clinical vital sign [15]. VO_2 max is a versatile metric; apart from risk stratification, it is used to guide exercise prescription for cardiac rehabilitation patients, to evaluate functional capacity before surgery, and to monitor disease progression in patients with heart failure and chronic obstructive pulmonary disease [16].

VO_2 max is also an essential metric in athletic settings. It has been shown to be a key determinant of exercise endurance performance and is routinely measured in elite athletes to guide training [17].

While endurance is affected by a plethora of factors, such as lactate threshold, running economy, and fractional utilization of VO_2 max, the maximum rate of oxygen consumption sets an upper limit on how much aerobic energy can be produced over time. Continuous, long-term monitoring of VO_2 max allows coaches and sport scientists to suggest appropriate training adaptations and identify periods of overtraining or detraining.

The standard method to measure VO_2 max is through indirect calorimetry performed during a graded exercise test [18]. The participating subject wears a mask or mouthpiece connected to a gas analysis system, which constantly measures the volume of inhaled and exhaled air along with the oxygen and carbon dioxide concentrations [19]. These measurements help estimate the oxygen consumption and carbon dioxide production per breath or over fixed time intervals [20]. The test is concluded when the subject reaches volitional exhaustion. VO_2 max is identified as a plateau in VO_2 even if the workload was increased, or it is identified by satisfying established secondary criteria such as respiratory exchange ratio exceeding 1.10 [16].

In the past, the most common method to measure VO_2 max was the Douglas bag method, but modern automated metabolic carts, such as the COSMED Quark CPET and the ParvoMedics TrueOne 2400 have replaced it [21–23]. These metabolic cart systems offer more advanced sensors and software, enabling real-time breath-by-breath data collection and analysis. Additionally, they provide a high degree of precision with only 2% to 5% test-retest coefficient of variation [24, 25]. Here are the major downsides of these systems: they are expensive, costing between $30,000 and $50,000 not including the recurring maintenance costs, and require trained operators to function effectively in controlled laboratory environments [21, 26]. The high cost and limited portability constrains VO_2 max testing to well-funded research facilities and privatized athletic institutions, leaving the majority of athletes, clinicians, and coaches without access to direct measurement [26]. Figures 1 and 2 show two widely used commercial metabolic cart systems.

B. Statement of the Problem

As previously mentioned, high equipment cost, the need for trained operators, and limited portability restrict direct VO_2 max measurement to well-funded research facilities and privatized athletic institu-

Figure 1. The COSMED Quark CPET, a stationary metabolic cart used for laboratory VO_2 max testing [1].

Figure 2. The ParvoMedics TrueOne 2400, a stationary metabolic cart widely used as a reference system in validation studies [2].

tions [21, 26]. Specialized clinics and university centers offer fee-for-service testing, but the cost per visit, typically exceeding $200 for the general public [27, 28], makes frequent monitoring financially unsustainable. As a result, resource-constrained individuals and organizations such as community health clinics, school athletic programs, personal trainers, and researchers in developing regions lack reliable access to this important metric.

There are several accessible methods to estimate maximal oxygen consumption without the use of expensive commercial metabolic carts. These methods include simple field tests called submaximal exercise protocols, such as the cooper 12-minute run test [29], the 20-meter shuttle run test [30], and cycle ergometer prediction equations [31]. While inexpensive and relatively easy to conduct, these tests rely on average population data and introduce high prediction errors ranging from 10% to 20% of the measured value [32]. Consequently, for personalized individual level assessment and clinical decision making, this lack of precision is often considered suboptimal.

Another accessible form of measuring VO_2 max is through consumer wearable devices. These wearable devices, such as the Apple Watch, Garmin, Whoop, etc. estimate VO_2 max using heart rate data and proprietary algorithms. While relatively inexpensive to own, these wearable devices estimate VO_2 max from submaximal heart rate responses rather than direct gas exchange measurement. Independent validation studies have shown mean errors of 8% to 15% compared to the criterion metabolic cart testing [33, 34]. Since these devices do not measure expired gas concentrations, they cannot deliver results consistently comparable to true indirect calorimetry.

Recently, portable metabolic analyzers have entered the market as alternatives to standard laboratory metabolic carts. The COSMED K5 is widely regarded as the gold standard for portable field metabolic analysis [3]. It uses a galvanic fuel cell O_2 analyzer (120 ms response time), an NDIR CO_2 analyzer (100 ms response time), and a bidirectional digital turbine flow sensor, supporting both mixing chamber and breath-by-breath measurement modes [3]. Validation studies have demonstrated group-level errors below 5% against Douglas bags [35] and accuracy approaching that of stationary metabolic carts [36]. However, the K5 weighs approximately 900 g, is worn on the back via a harness with a sampling line running to a face mask, and costs an estimated $25,000 to $45,000 [3]—placing it in a similar price category to stationary systems.

At a lower price point, the VO2 Master Pro is a mask-worn device that performs gas exchange measurement using an onboard O_2 sensor (though notably lacking a CO_2 sensor) and Bluetooth connectivity to a companion web application. Weighing approximately 325 g, it is more compact than the K5 [4]. When tested against a reference laboratory cart (ParvoMedics TrueOne 2400), the VO2 Master Pro showed strong correlations ($r = 0.97$) for VO_2 during submaximal exercise. However, mean absolute percent errors reached approximately 12% during maximal testing, and test-retest reliability was lower than the reference cart [26]. Its price of $6,800 to $8,000 remains a barrier for many individuals and organizations [4]. Figures 3 and 4 show both portable systems.

Figure 3. The COSMED K5 portable metabolic analyzer, worn on the back via a harness with a sampling line to a face mask [3].

A few hobbyist and open-source communities have attempted to build lower-cost metabolic measurement systems using commercially available equipment, sensors and microcontrollers. However, most of these projects are limited to proof-of-concept prototypes with incomplete or entirely missing validation data, a lack of open-source hardware and software pipeline, and restricted sensor choices

Figure 4. The VO2 Master Pro, a self-contained mask-worn portable metabolic analyzer [4].

[37]. Consequently, there exists no widely available validated, low-cost portable system that combines expired air concentration analysis with air flow measurement.

This thesis addresses the lack of an affordable, portable system for direct VO_2 max measurement. The prohibitive cost associated with commercial metabolic carts prevents the widespread use of the VO_2 max metric and indirect estimation approaches do not provide the level of precision required for clinical or individualized applications.

C. Purpose and Scope

The purpose of this study is to design, build, and validate a low-cost and portable system for measuring VO_2 max through direct exhaled gas analysis. The system is meant to serve as an affordable and accessible alternative to commercial metabolic carts by using off-the-shelf sensors, a custom 3D-printed enclosure incorporating two one-way-valves for separating the inhaled and exhaled air, and a venturi tube for airflow measurement, and open-source firmware and software. This design costs a fraction of the price of both commercially available metabolic carts and existing portable analyzers such as the

COSMED K5 and VO2 Master Pro, while still employing the same underlying indirect calorimetry measurement principle used by laboratory-grade systems [38].

The system measures the three quantities required for computing VO_2 through indirect calorimetry: volumetric airflow, expired oxygen concentration, and expired carbon dioxide concentration [38]. The custom 3D-printed venturi tube measures airflow by relating the difference in pressure between its inlet and a constricted throat section to the flow rate based on Bernoulli's principle. Venturi-based flow measurement is heavily used in industrial applications and recently has been shown to be a viable method for respiratory flow measurement in low-cost spirometry devices [39]. An inexpensive ESP32 microcontroller connects with O_2, CO_2 and differential air pressure sensors to measure gas concentrations and pressure levels in the exhaled air. Bluetooth Low Energy (BLE) is used to transmit the data wirelessly to a Python-based data logging and analysis pipeline which handles breath detection, flow rate computation, and VO_2 calculation. This design methodology not only prioritizes affordability and portability, but also allows reproducibility and open-source development.

At the time of writing, Institutional Review Board approval has not been obtained and a reference flow standard (calibration syringe or spirometer) was not available. Therefore, all validation is limited to instrument-level characterization. Each sensor is verified independently: the carbon dioxide sensor is tested through controlled elevation and recovery cycles in a sealed chamber, the oxygen sensor through displacement and recovery tests, and the differential pressure sensor through zero-flow stability and airflow response characterization. A stoichiometric reaction of vinegar and baking soda is employed to simultaneously elevate CO_2 and displace O_2, allowing for the verification of sensor response and dynamic range [40]. System integration testing verifies the complete data pipeline from sensor acquisition through wireless transmission to data logging and analysis. Because no reference flow standard was available, the Venturi discharge coefficient is not empirically determined; a literature-based estimate is used for flow rate calculations. This instrument-level approach establishes a characterized hardware and software platform that is ready for calibration with a reference flow standard and human subject testing once IRB approval is obtained.

There are several limitations to note. Only a single prototype of the system has been built and tested, so manufacturing reproducibility across multiple units has not been characterized. The 3D-

printed Venturi tube is subject to manufacturing tolerances that may affect dimensional accuracy and surface finish, both of which influence the discharge coefficient. The electrochemical oxygen sensor has a response time of 2 seconds, which is considerably slower than the sensors used in commercial metabolic carts [21, 41]. This slower response time may limit accuracy during high-frequency breathing associated with intense exercise. The carbon dioxide sensor updates at approximately 0.5 Hz, presenting a similar constraint. A more detailed discussion of these hardware limitations and their effects on measurement accuracy is provided in Chapter V.

Despite these constraints, this thesis provides a fully documented and reproducible platform with characterized measurement accuracy for each sensor component. The instrument-level validation establishes the measurement foundation required before proceeding to human subject testing [42]. The open-source nature of both the hardware design and software pipeline allows other researchers to replicate, modify, and extend the system for their own applications.

D. Significance of the Study

The significance of this study lies in its potential to make direct VO_2 max measurement accessible to individuals and organizations that currently cannot afford commercial alternatives. As established in earlier sections, the cost of both laboratory-grade and portable metabolic systems places direct measurement out of reach for most clinical and athletic settings. A validated low-cost system using off-the-shelf components could significantly lower this barrier.

The clinical case for broader access to VO_2 max testing is strong. Given that cardiorespiratory fitness is a stronger predictor of all-cause mortality than traditional risk factors [13, 14] and that the American Heart Association has recommended it be assessed as a clinical vital sign [15], incorporating direct VO_2 max measurement into routine clinical practice has clear value. However, doing so remains impractical when the most accurate measurement method requires equipment costing tens of thousands of dollars. A low-cost portable system could enable clinicians to incorporate direct measurement into routine patient assessments, particularly in community health settings and cardiac rehabilitation programs [16].

Beyond the clinical applications, in athletic settings, VO_2 max monitoring guides training decisions [17], the cost of metabolic carts limits access primarily to well-funded programs. A portable and affordable device could enable routine metabolic testing in the field, which is particularly relevant for high school and collegiate programs that typically lack the budget for commercial equipment.

Finally, this thesis contributes a complete and documented methodology for building and validating a low-cost respiratory gas analysis system. The hardware designs, firmware, data logging tools, and analysis scripts are all openly available, and the Venturi tube can be reproduced using standard 3D printers. By providing detailed documentation of the design rationale, verification procedures, and sensor characterization results, this work offers a practical starting point for other researchers and developers interested in building affordable metabolic measurement systems. This stands in contrast to previous low-cost attempts that have lacked rigorous validation or sufficient documentation for reproducibility [37].

E. Organization of the Thesis

The remainder of this thesis is organized into five chapters. Chapter II reviews the relevant literature, covering the physiology of VO_2 max, existing measurement modalities, Venturi flow theory, sensor technologies for respiratory gas analysis, and instrument validation methodologies. Chapter III presents the system design and implementation, including the Venturi tube geometry, electronic component selection and circuit design, firmware development, the Python-based data logging and analysis pipeline, and the physical assembly of the prototype. Chapter IV describes the sensor verification and characterization methodology, presenting results from individual sensor tests and a system integration test. Chapter V discusses the interpretation of sensor dynamics, evaluates whether the system meets its design constraints, and assesses the reliability of the verification methods used. Chapter VI concludes with challenges and limitations, an assessment of system readiness, and recommendations for future work.

CHAPTER II.

LITERATURE REVIEW

A. Physiology of Maximal Oxygen Consumption

The physiological basis for measuring VO_2 max rests on the Fick equation, first described by Adolf Fick in 1870 [43, 44]:

$$\dot{V}O_2 = \dot{Q} \times (C_aO_2 - C_{\bar{v}}O_2) \tag{2.1}$$

where $\dot{Q}$ is cardiac output, C_aO_2 is the arterial oxygen content, and $C_{\bar{v}}O_2$ is the mixed venous oxygen content. The equation shows that VO_2 is governed by two factors: how much blood the heart can pump and how much oxygen the muscles can extract from that blood [10]. Of these two factors, research has consistently identified cardiac output as the primary limiter of VO_2 max in healthy individuals at sea level [10, 45].

As introduced in Chapter I, a true VO_2 max is confirmed by a plateau in oxygen consumption despite increasing workload, or by secondary criteria such as a respiratory exchange ratio exceeding 1.10 [16]. Taylor et al. formalized the plateau criterion in 1955, defining it as an increase of less than 150 mL/min (approximately 2.1 mL/kg/min) in VO_2 despite an increase in workload [46]. Since not all subjects demonstrate a clear plateau, the secondary criteria, including age-predicted maximal heart rate and rating of perceived exertion, serve as practical alternatives for confirming maximal effort [16, 38].

Crucially, the oxygen consumed at the tissue level as described by the Fick equation must, at steady state, equal the oxygen removed from inhaled air at the lungs [38]. This mass-balance principle means that VO_2 can be determined entirely from ventilatory measurements: by comparing the volume and oxygen concentration of inspired air with those of expired air, one can calculate how much oxygen was retained by the body during each breath without requiring blood sampling or cardiac output measurement. This insight—that gas exchange at the mouth faithfully reflects metabolic gas exchange at the tissues—is the foundation of indirect calorimetry and the basis for every portable metabolic system, including the one developed in this thesis. Accordingly, a practical VO_2 max measurement

system must measure both ventilatory volume and expired gas concentrations with sufficient precision to detect physiologically meaningful changes in VO_2 during graded exercise.

B. Methods of Measuring VO_2 max

There are two fundamental approaches for measuring metabolic rate: direct calorimetry and indirect calorimetry. Direct calorimetry measures metabolic rate by quantifying the heat produced by the body inside an insulated chamber. While historically important for establishing the relationship between oxygen consumption and energy expenditure, direct calorimetry requires a sealed room-sized apparatus and cannot be practically applied during exercise testing [38]. Indirect calorimetry instead infers metabolic rate from respiratory gas exchange by measuring the volume of oxygen consumed and carbon dioxide produced. As described in Chapter I, this is the standard approach for VO_2 max testing and the measurement principle used by all modern metabolic analysis systems [21]. Indirect calorimetry can be performed in two configurations: closed-circuit systems, in which the subject rebreathes from a sealed supply of oxygen while exhaled CO_2 is chemically absorbed, and open-circuit systems, in which the subject inhales ambient air and the expired gas is analyzed for its O_2 and CO_2 concentrations [38]. All modern metabolic carts and portable analyzers, including the system developed in this thesis, use the open-circuit configuration.

The earliest practical implementation of open-circuit indirect calorimetry was the Douglas bag method [47], which collected expired gas in a large bag for subsequent volume measurement and chemical analysis. Although it served as the reference standard for nearly a century, the Douglas bag is labor-intensive and provides only batch-averaged values rather than real-time data [48].

The transition to automated measurement systems produced two principal operating modes: mixing chamber and breath-by-breath [48]. In mixing chamber mode, expired gas flows into a homogenizing chamber while a separate flow sensor measures total ventilation; gas concentrations are sampled at regular intervals and multiplied by ventilation to compute VO_2. Breath-by-breath mode instead uses fast-response gas analyzers synchronized with a flow sensor to measure gas concentrations and airflow simultaneously, computing gas exchange for each individual breath cycle. Breath-by-breath analysis

provides much higher temporal resolution and has become the dominant mode in modern metabolic carts, though it places stricter requirements on sensor response time and signal alignment [48].

Regardless of the operating mode, a fundamental challenge in open-circuit indirect calorimetry is that the volume of inspired air (V_I) differs from the volume of expired air (V_E) because the body typically consumes more oxygen than it produces carbon dioxide. The ratio of CO_2 produced to O_2 consumed is the respiratory exchange ratio (RER), which ranges from approximately 0.7 during fat oxidation to 1.0 during pure carbohydrate oxidation [38]. At any RER below 1.0, the expired volume is smaller than the inspired volume. Since most open-circuit systems measure only expired gas flow and composition, the inspired volume must be derived indirectly. The Haldane transformation provides this derivation by assuming that nitrogen is metabolically inert: the volume of N_2 inspired must equal the volume expired [38]. Expressing the nitrogen fractions as $F_iN_2 = 1 - F_iO_2 - F_iCO_2$ and $F_eN_2 = 1 - F_eO_2 - F_eCO_2$, the nitrogen balance $V_I \times F_iN_2 = V_E \times F_eN_2$ yields:

$$V_I = V_E \times \frac{1 - F_eO_2 - F_eCO_2}{1 - F_iO_2 - F_iCO_2} \tag{2.2}$$

This allows VO_2 and VCO_2 to be computed entirely from expired gas measurements and the known composition of ambient inspired air. The Haldane transformation is used by virtually all modern metabolic measurement systems [21] and is applied in the computation methodology described in Chapter III.

1. Commercial metabolic cart systems

Modern automated metabolic carts, such as the systems mentioned in Chapter I, typically combine a pneumotachograph or turbine flow sensor with a fast-response paramagnetic O_2 analyzer and an NDIR CO_2 analyzer [48]. The gas analyzers in these systems have response times below 100 milliseconds, which is necessary to track the rapid changes in gas concentration within a single breath during breath-by-breath analysis. This requirement for fast-response, high-precision sensors is one of the primary drivers of the high cost associated with these systems [21]. Additionally, commercial carts require

regular calibration with certified reference gas mixtures and a volume calibration syringe [21], adding to operational complexity and recurring expense.

The measurement precision of breath-by-breath systems depends on accurate synchronization between the flow and gas concentration signals. Even small timing errors between the flow sensor and gas analyzers can introduce significant errors in the computed gas exchange values, since the calculation requires multiplying instantaneous flow by instantaneous gas concentration [48]. Commercial systems address this through proprietary delay-correction algorithms, but the sensitivity to timing errors remains a recognized source of measurement variability. Test-retest coefficients of variation for commercial breath-by-breath systems typically range from 2% to 5% [41], and Meyer et al. demonstrated that systematic differences can arise even between two carts from the same manufacturer [49].

2. Low-cost and portable alternatives

Efforts to miniaturize laboratory metabolic carts have produced portable breath-by-breath analyzers that can be worn on the body. The COSMED K5, the current gold standard for portable field metabolic analysis, uses medical-grade galvanic fuel cell and NDIR sensors with response times of 100–120 ms and achieves group-level errors below 5% against Douglas bags [3, 35, 36]. However, it weighs approximately 900 g, requires a back-mounted harness with a sampling line to a face mask, and costs an estimated $25,000 to $45,000. Lower-cost alternatives such as the VO2 Master Pro ($6,800–$8,000) reduce size but sacrifice sensor coverage and accuracy [4, 26]. Existing low-cost hobbyist efforts have lacked rigorous calibration and validation. This cost-accessibility gap motivates the system developed in the present work.

C. Venturi Flow Measurement Theory

A Venturi tube is a converging duct that measures volumetric flow rate by creating a measurable pressure drop at a constricted throat section. The operating principle follows from two fundamental laws of fluid mechanics: the continuity equation (conservation of mass) and Bernoulli's equation (conservation of energy along a streamline) [50]. For steady, incompressible, inviscid flow through a horizontal

duct, Bernoulli's equation states:

$$P_1 + \tfrac{1}{2}\rho v_1^2 = P_2 + \tfrac{1}{2}\rho v_2^2 \tag{2.3}$$

where P_1 and P_2 are the static pressures at the inlet and throat, v_1 and v_2 are the corresponding flow velocities, and ρ is the fluid density. The continuity equation, $A_1 v_1 = A_2 v_2$, relates the velocities at the two cross-sections through their respective cross-sectional areas of the inlet (A_1) and the throat (A_2). Combining these two equations and solving for the volumetric flow rate $Q = A_2 v_2$ yields:

$$Q = A_2 \sqrt{\frac{2\,\Delta P}{\rho\,(1 - \beta^4)}} \tag{2.4}$$

where $\Delta P = P_1 - P_2$ is the measured differential pressure and $\beta = d_2/d_1$ is the diameter ratio of the throat to the inlet [50]. This equation represents the ideal case and assumes no viscous losses or flow non-uniformities.

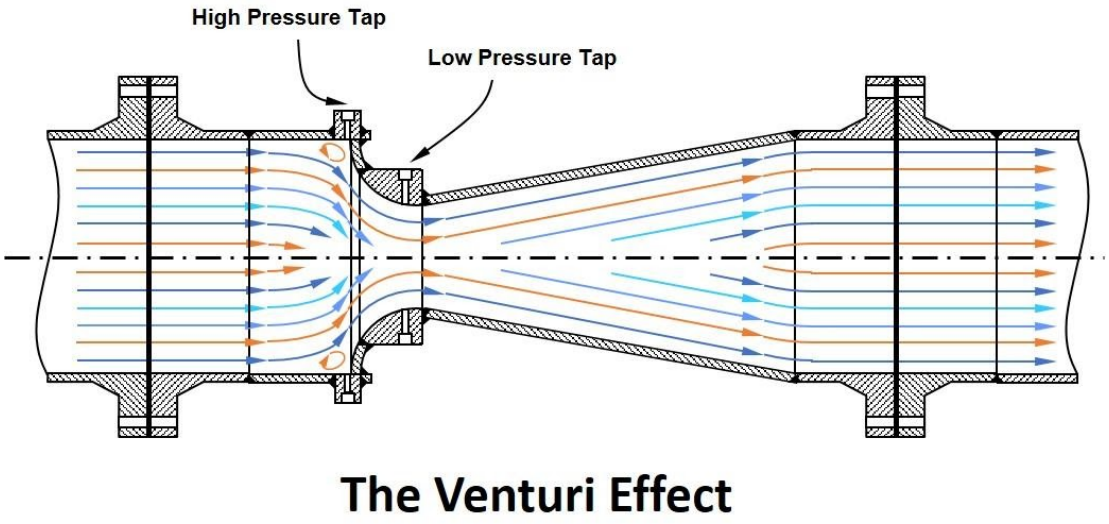

Figure 5. Cross-section of a Venturi tube showing the converging section, throat, and diverging section. Flow streamlines accelerate through the throat, producing a pressure drop between the high-pressure and low-pressure taps [5].

In practice, real flows experience viscous friction, boundary layer effects, and flow profile non-uniformities that cause the actual flow rate to be lower than the ideal prediction. These losses are accounted for by introducing an empirical discharge coefficient C_d into the flow equation:

$$Q = C_d \cdot A_2 \sqrt{\frac{2\,\Delta P}{\rho\,(1-\beta^4)}} \tag{2.5}$$

The discharge coefficient is defined as the ratio of the actual flow rate to the ideal flow rate and is always less than or equal to unity. For well-designed Venturi tubes that conform to the geometries specified in ISO 5167-4, C_d values typically range from 0.95 to 0.99 [51]. For non-standard geometries, such as 3D-printed tubes with smaller dimensions than those covered by the standard, C_d must be determined empirically through calibration against a reference flow measurement device. The discharge coefficient may also vary with flow rate, since viscous effects become more significant at lower Reynolds numbers [50].

The key geometric parameters that influence Venturi tube performance are the diameter ratio β, the convergent half-angle, and the pressure tap locations [50, 51]. Together, these parameters govern the trade-off between measurement sensitivity and flow resistance, as well as the stability of C_d across the operating range. The specific geometry selected for the system developed in this thesis and the rationale for each parameter are discussed in Chapter III.

The standard flow sensor in clinical spirometry is the pneumotachograph, which measures flow by sensing the pressure drop across a resistive mesh or capillary bundle [42]. However, these fine internal structures are susceptible to moisture accumulation from exhaled air and are difficult to manufacture inexpensively. Venturi tubes offer an alternative with no internal obstructions, making them inherently moisture-resistant and amenable to low-cost 3D printing. Recent studies confirm the viability of this approach: Nunes et al. achieved intraclass correlation coefficients above 0.85 with a 3D-printed Venturi spirometer [39], and Sridevi et al. demonstrated a low-cost Venturi spirometer for diagnosing chronic obstructive pulmonary disease [52].

A challenge in applying Venturi flow measurement to respiratory gas analysis is that breathing produces pulsatile rather than steady-state flow, with rapid transitions between inhalation and exhalation

that intensify during heavy exercise [42]. Systems that expose the Venturi tube to both inhaled and exhaled air must contend with bidirectional flow reversal, which can affect the discharge coefficient. However, designs that separate the inhale and exhale pathways using one-way valves, like the system described in Chapter III, can eliminate flow reversal through the Venturi tube entirely. The tube experiences only unidirectional exhalation flow alternating with periods of zero flow, a substantially less demanding condition. Additionally, exhaled air differs from ambient air in temperature, humidity, and gas composition, all of which affect the density term ρ in Equation 2.5 [50]. Chapter III describes how the system accounts for these variations using real-time temperature and humidity measurements from the SCD30 sensor.

D. Sensor Technologies for Respiratory Gas Analysis

Two principal technologies are used for measuring oxygen concentration in respiratory gas analysis: paramagnetic analyzers and galvanic electrochemical sensors [53]. Paramagnetic analyzers exploit the fact that oxygen molecules have unpaired electrons, making them attracted to magnetic fields. A rapidly switching electromagnetic field causes oxygen molecules to oscillate, producing a pressure signal proportional to the oxygen partial pressure in the gas sample [53]. These analyzers achieve response times below 100 milliseconds and high measurement precision, which is why they are the standard in laboratory metabolic carts as noted in Section B. However, paramagnetic analyzers are expensive, sensitive to mechanical vibration, and require frequent calibration with certified reference gas mixtures [48].

Galvanic electrochemical oxygen sensors offer a substantially lower-cost alternative to paramagnetic analyzers. In these sensors, oxygen diffuses through a permeable membrane to a cathode where it is reduced in an electrochemical reaction, while a sacrificial anode (typically lead) is simultaneously oxidized [53]. The resulting electrical current is proportional to the partial pressure of oxygen in the sample gas. Advantages of electrochemical sensors include self-powered operation requiring no external excitation voltage, low cost, compact size, and a linear output signal. The main limitations are slower response times compared to paramagnetic sensors, a finite operational lifespan of one to two years as the anode material is consumed, temperature sensitivity, and susceptibility to baseline drift

requiring periodic recalibration [21]. The slower response time means that electrochemical sensors are less suited to true breath-by-breath analysis, but they remain viable when the measurement methodology accommodates their temporal characteristics through averaging or post-processing approaches.

Nondispersive infrared (NDIR) sensing is the dominant technology for carbon dioxide measurement in both laboratory and portable metabolic systems. The operating principle is based on the Beer-Lambert law: CO_2 molecules absorb infrared radiation at a characteristic wavelength of 4.26 μm, and the degree of absorption is proportional to both the gas concentration and the optical path length [8]. A typical NDIR sensor consists of an infrared source, a sample chamber through which the gas flows or diffuses, an optical bandpass filter centered at the CO_2 absorption wavelength, and an infrared detector. NDIR sensors offer excellent long-term stability, high selectivity for CO_2, and no consumable components unlike electrochemical sensors. Response time depends on the sample chamber design: laboratory-grade mainstream analyzers positioned directly in the breathing circuit achieve fast response comparable to paramagnetic oxygen sensors, while compact modules that rely on gas diffusion into an enclosed measurement chamber have inherently slower response [48].

Differential pressure sensors are required for Venturi-based flow measurement, as described in Section C. Modern microelectromechanical systems (MEMS) differential pressure sensors commonly use a thermal calorimetric sensing principle: a micro-heater on a silicon membrane creates a temperature profile, and airflow across the membrane displaces this profile asymmetrically. Upstream and downstream temperature sensors detect this displacement, producing a signal proportional to the pressure difference [6]. MEMS sensors of this type offer high sensitivity at low differential pressures with sub-Pascal resolution, digital output interfaces such as I^2C, and compact packaging. For respiratory applications, the sensor must resolve the small pressure differentials generated during quiet breathing while also handling the larger pressures produced during forced exhalation. The sampling rate is also important because it must be sufficient to capture the temporal dynamics of each breath cycle for accurate flow integration [6].

The selection of sensor technologies for a low-cost respiratory gas analysis system involves fundamental trade-offs between cost, response time, accuracy, and power consumption. As discussed in Section B, commercial metabolic carts achieve breath-by-breath precision using expensive fast-

response paramagnetic oxygen analyzers and mainstream NDIR carbon dioxide analyzers. A low-cost system must use less expensive alternatives and adapt the measurement methodology to accommodate their slower response characteristics, as discussed above. The specific sensor selections made for the system developed in this thesis and the rationale behind those choices are presented in Chapter III.

E. Instrument Validation Methodologies

The ATS/ERS standardization of spirometry requires that flow-measuring devices be calibrated using a 3.00 L calibration syringe, with an acceptable volume accuracy of $\pm 3.5\%$ or ± 50 mL, whichever is greater [42]. For differential-pressure flow meters such as Venturi tubes, this procedure simultaneously validates volume accuracy and provides the data needed to determine the empirical discharge coefficient C_d introduced in Section C [51]. The syringe is pumped at multiple flow rates spanning the expected respiratory range to characterize C_d across the operating envelope.

Rather than calibrating each sensor component in isolation, an integrated approach passes a known reference input through the complete measurement path and derives a single lumped correction factor that accounts for all deviations from ideal behavior: sensor nonlinearity, geometric manufacturing tolerances, and fluid property variations [51]. Nunes et al. used this approach when validating their 3D-printed Venturi spirometer, comparing measured volumes directly against a reference spirometer rather than calibrating the pressure sensor in isolation [39].

As noted in Section B, gas sensor calibration in commercial metabolic carts uses certified reference gas mixtures [48]. The standard protocol is a two-point calibration: for oxygen, ambient air at 20.93% serves as one point while a certified low-O_2 mixture (typically 15–16%) provides the second; for carbon dioxide, ambient air at approximately 420 ppm serves as the baseline and a certified 4–5% CO_2 mixture provides the span [21]. An alternative approach uses controlled chemical reactions to generate reference gas environments. Acid-base reactions such as acetic acid with sodium bicarbonate produce CO_2 while displacing O_2 in a sealed container, providing extreme reference points for both sensors simultaneously [40]. Combined with ambient air as the opposing calibration point, this yields a two-point verification using inexpensive reagents. The steady-state concentrations depend on reaction

stoichiometry and container volume, so the extreme endpoints are less precisely characterized than certified mixtures, but they are sufficient for verifying sensor linearity and dynamic range.

Any instrument validation must quantify measurement uncertainty. The Guide to the Expression of Uncertainty in Measurement distinguishes Type A uncertainty, evaluated by statistical analysis of repeated measurements, from Type B uncertainty, evaluated from sensor datasheets and calibration tolerances [54]. Both types propagate through the VO_2 computation, so flow and gas concentration uncertainties each contribute to the final result. Test-retest coefficients of variation for commercial metabolic carts are typically reported in the range of 2% to 5% [41], establishing a practical accuracy benchmark for evaluating alternative systems.

F. Summary and Research Gap

This chapter has established the measurement chain required for a low-cost VO_2 max system. The Fick equation links VO_2 to cardiovascular function at the tissue level, but the mass-balance principle allows the same quantity to be determined entirely from respiratory gas exchange at the mouth, without invasive blood sampling. Open-circuit indirect calorimetry implements this principle by measuring expired airflow and gas concentrations, with the Haldane transformation accounting for the volume difference between inspired and expired air. Commercial metabolic carts achieve high precision using fast-response paramagnetic analyzers and pneumotachographs, but at costs that limit accessibility. Venturi-based differential pressure sensing provides a low-cost, moisture-resistant flow measurement alternative amenable to 3D printing, while electrochemical O_2 sensors and NDIR CO_2 sensors offer affordable substitutes for laboratory-grade gas analyzers—each with response time trade-offs that must be accommodated through the measurement methodology. Established validation approaches, including syringe-based flow calibration and controlled chemical reaction gas verification, provide a framework for characterizing such a system with quantified uncertainty.

What is missing from the current literature is a fully documented, open-source, low-cost system that integrates these sensing technologies into a functional prototype with calibration data and quantified measurement uncertainty. This thesis addresses that gap.

CHAPTER III.

SYSTEM DESIGN AND IMPLEMENTATION

A. Design Requirements and Constraints

The primary goal of this system is to measure the three quantities required for computing VO_2 through indirect calorimetry: volumetric airflow, expired oxygen concentration, and expired carbon dioxide concentration [38]. These quantities fluctuate significantly during exercise, and the expected measurement ranges are determined by human respiratory physiology. Respiratory flow rates during exercise range from near zero at rest to peak values approaching 200 L/min during maximal exertion, though sustained minute ventilation during heavy exercise typically falls between 60 and 120 L/min [38]. Expired oxygen concentration drops from approximately 20.93% (ambient) to approximately 16% during intense exercise, while expired carbon dioxide concentration rises from approximately 3.5% (35,000 ppm) at rest to approximately 5% (50,000 ppm) at maximal effort [38]. The sensors must therefore cover a wide measurement range, from ambient baselines (0.04% CO_2, 20.93% O_2) through peak expired concentrations, while providing resolution sufficient to compute meaningful VO_2 values.

Unlike commercial metabolic carts, which operate in a stationary laboratory environment without portability constraints, the system presented in this thesis operates under strict size, weight, power, and budget constraints. These constraints are necessary to enable field-based data collection and to lower the economic barrier to VO_2 max measurement, thereby making this vital clinical metric accessible to a wider range of users. Consequently, these strict design limitations fundamentally influenced the architectural design decisions described in the remainder of this chapter.

B. System Architecture Overview

To address the requirements and constraints outlined in Section A, the system is organized into three subsystems: a 3D-printed mechanical enclosure, an electronic sensor and data acquisition platform, and a software pipeline for data logging and analysis. Figure 6 presents the end-to-end signal chain

from the wearable hardware through wireless transmission, data logging, post-processing, and final computed outputs.

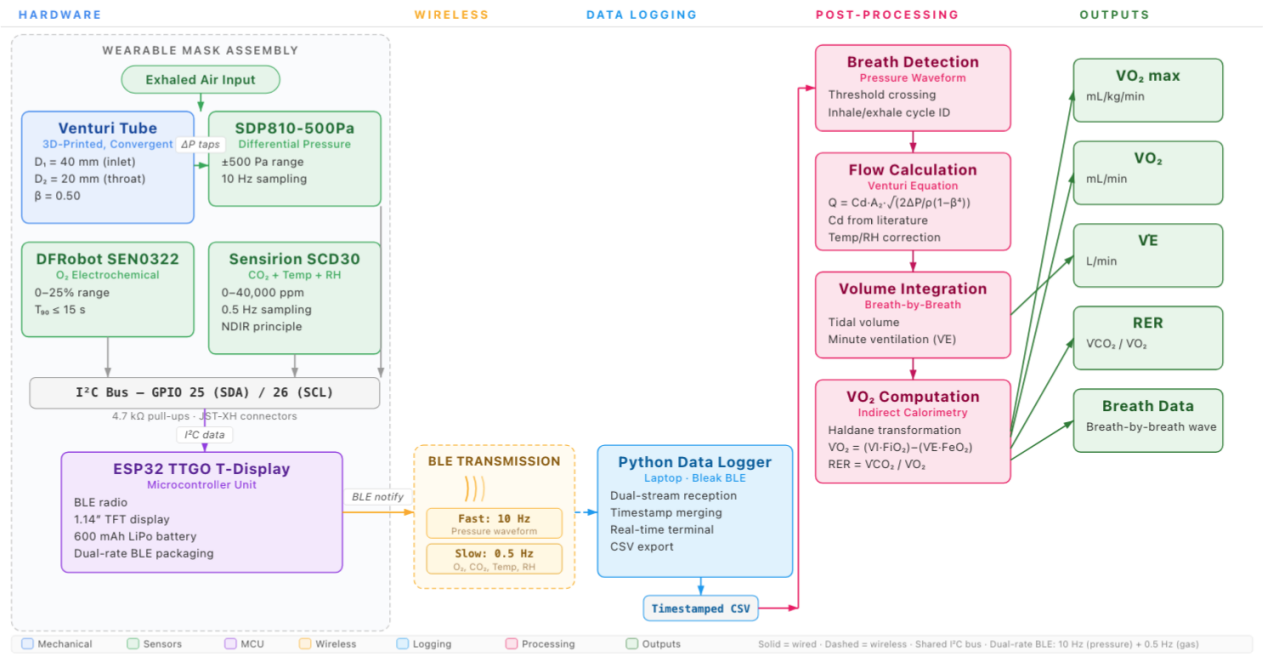

Figure 6. System overview showing the complete data pipeline from the wearable mask assembly through BLE transmission, Python-based data logging, offline post-processing, and computed metabolic outputs.

1. Mechanical architecture

The physical design consists of three modular 3D-printed compartments joined by threaded M5 interfaces: a left compartment housing the microcontroller, battery, and circuit board; a central compartment that connects to the mask cushion and contains the one-way valves separating the inhale and exhale airflow paths; and a right compartment containing the Venturi tube and all three sensors. This modular approach allowed individual compartments to be revised and reprinted independently as the

design evolved through multiple iterations, without discarding the rest of the assembly. The enclosure geometry and fabrication details are described in Sections C and G.

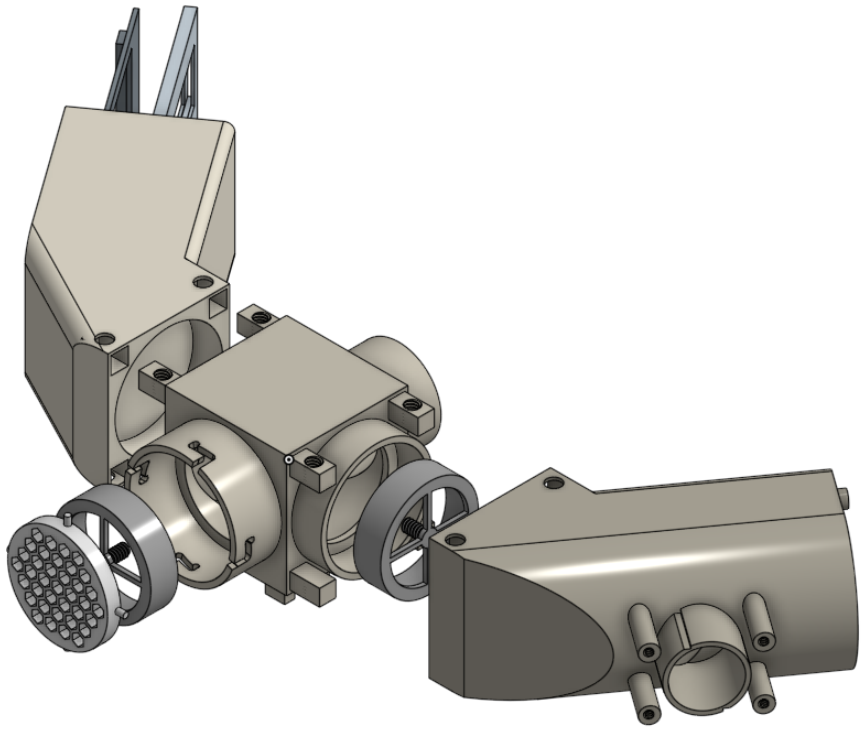

Figure 7. Isometric CAD rendering of the three modular 3D-printed compartments. From left to right: the electronics housing, the central valve and mask interface, and the sensor compartment containing the Venturi tube.

2. Electronic hardware

The electronic hardware uses commercially available off-the-shelf sensors connected to an ESP32 microcontroller over a shared I^2C bus. The sensor selections were inspired by a prior open-source effort [37] and retained because the low-cost sensor market has not produced meaningfully better alternatives at comparable price points in the past 5 years. The system is powered by a single 600mAh

lithium-ion battery, chosen for its compact form factor and sufficient energy density for the duration of a typical exercise test.

Electronics assembly is done through perfboard prototyping with soldered connections rather than custom printed circuit board fabrication. To enhance modularity and facilitate maintenance, sensors are connected via wires of varying lengths terminated with 4-pin JST XH connectors. This interconnect strategy allows individual sensors to be disconnected and replaced without desoldering, while the custom wire lengths ensure optimal cable management within the compact enclosure. The microcontroller, sensor choices, and circuit layout are detailed in Section D.

3. Software pipeline

During early development, I tried to perform gas exhange computation directly on the microcontroller similar to the approach taken in a prior open-source project [37]. However, accurately aligning the asynchronous sensor streams, specifically the slow response of the gas sensors relative to the instantaneous flow sensor, proved unreliable on the embedded platform.

Additionally, iterating on signal processing algorithms in embedded C++ was inefficient due to the lack of immediate data visualization tools and the overhead of the build-upload-test cycle. As a result, the architecture was revised to a telemetry-based model where the firmware is limited to sensor polling and wireless data transmission via Bluetooth Low Energy. All complex signal processing and VO_2 computations are offloaded to a Python application running on an external more computationally powerful system, allowing for the use of high-level analysis libraries (e.g., NumPy, Pandas, Matplotlib) and rapid tuning of breath detection parameters. This division of labor is detailed in Sections E and F.

Table I lists the major components and their approximate costs. The total bill of materials is approximately $222, which is less than 1% of the cost of a commercial metabolic cart or the COSMED K5 portable analyzer ($25,000–$45,000) and roughly 3% of the VO2 Master Pro ($6,800–$8,000) [3, 4, 21].

Table I. BILL OF MATERIALS AND APPROXIMATE COMPONENT COSTS

Component	Estimated Cost (USD)
CPAP mask cushion	$30
ESP32 TTGO T-Display V1.1	$10
Sensirion SDP810-500Pa	$53
DFRobot Gravity O_2 sensor (SEN0322)	$54
Sensirion SCD30	$62
PETG filament ($\sim$200 g)	$5
Li-ion battery (3.7 V)	$8
Total	**$222**

C. Venturi Tube Design and Fabrication

Chapter II established the theoretical basis for Venturi flow measurement: Bernoulli's equation combined with the continuity equation yields the flow rate from the measured differential pressure (Equation 2.5), with the empirical discharge coefficient C_d accounting for viscous losses and geometric imperfections. This section describes the specific geometry chosen for the system and the rationale behind each design parameter. The Venturi tube is a converging-only duct 3D-printed as a single piece within in the right compartment of the enclosure. Its geometry was designed to produce measurable pressure drops across the expected range of respiratory flow rates while minimizing breathing resistance.

1. Inlet and throat dimensions

The inlet diameter was set to $D_1 = 40$ mm and the throat diameter to $D_2 = 20$ mm, giving a diameter ratio of $\beta = D_2/D_1 = 0.50$ and an area ratio of $\beta^2 = 0.25$.

The choice of $\beta = 0.50$ represents a balance between measurement sensitivity and flow resistance. Smaller values of β produce larger pressure drops for a given flow rate, improving the signal-to-noise ratio at low flow rates. However, a smaller throat also increases the resistance to breathing; this parameter may be revisited once human subject testing is conducted pending IRB approval. The

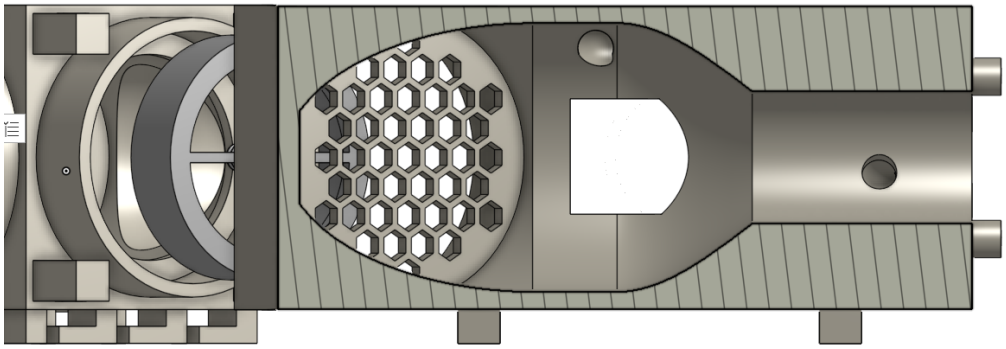

Figure 8. Cross-section of the enclosure showing the one-way valves, honeycomb flow straightener, and converging Venturi tube with pressure tap ports.

expected pressure drop at a given volumetric flow rate Q can be estimated by rearranging Equation 2.5:

$$\Delta P = \frac{\rho\,(1-\beta^4)}{2}\left(\frac{Q}{C_d \cdot A_2}\right)^2 \tag{3.1}$$

The throat cross-sectional area is computed from the throat diameter:

$$A_2 = \pi\left(\frac{D_2}{2}\right)^2 = \pi\left(\frac{0.020}{2}\right)^2 = \pi\,(0.010)^2 = 3.14 \times 10^{-4}\ \text{m}^2 \tag{3.2}$$

Using approximate room-temperature air density $\rho = 1.2$ kg/m^3, an initial discharge coefficient estimate of $C_d \approx 0.97$, and $\beta^4 = (0.50)^4 = 0.0625$, the expected pressure drop can be evaluated at two representative flow rates.

At a moderate exhalation of $Q = 60$ L/min $= 1.0 \times 10^{-3}$ m^3/s:

$$\Delta P = \frac{1.2\,(1-0.0625)}{2}\left(\frac{1.0 \times 10^{-3}}{0.97 \times 3.14 \times 10^{-4}}\right)^2 \approx 5.5\ \text{Pa} \tag{3.3}$$

At a peak exercise flow rate of $Q = 200$ L/min $= 3.33 \times 10^{-3}$ m^3/s:

$$\Delta P = \frac{1.2\,(1 - 0.0625)}{2} \left(\frac{3.33 \times 10^{-3}}{0.97 \times 3.14 \times 10^{-4}} \right)^2 \approx 61 \text{ Pa} \tag{3.4}$$

Both values fall well within the 500 Pa range of the SDP810 differential pressure sensor described later in this section, while the lower end remains above the sensor's 0.1 Pa resolution.

2. Convergence angle and throat length

The convergent half-angle was set to 21 degrees, which is steeper than the 10.5-degree half-angle specified for standard industrial Venturi tubes in ISO 5167-4 [51]. This departure from the standard was driven by the portability constraint: a 10.5-degree half-angle with the same inlet and throat diameters would require a convergent section approximately 27 mm long, whereas the 21-degree angle reduces this to approximately 13 mm. This reduction in overall length is important because the Venturi tube must fit inside a mask-mounted enclosure where space is limited.

The steeper angle introduces a trade-off. Theoretically, a more gradual convergence allows the boundary layer to remain attached to the wall, producing a more uniform velocity profile at the throat and a more predictable discharge coefficient [50]. Steeper angles increase the risk of flow separation at the convergent-throat junction, which can increase turbulence and lower C_d [55]. However, since C_d will ultimately be determined empirically through calibration with a reference flow standard rather than predicted from the ISO correlation [51], a moderately steeper angle is acceptable provided that C_d remains repeatable across the operating flow range.

The throat section has a length of 32.5 mm, which provides approximately 1.6 throat diameters of straight duct. This length allows partial flow development in the throat before the pressure tap location, improving the stability of the pressure measurement.

3. Pressure tap placement

Two pressure taps are integrated into the Venturi tube walls to connect the differential pressure sensor as visible in Figure 8. The upstream tap (P1) is located 3 mm before the start of the convergent section, where the flow is still in the full-diameter inlet and is relatively undisturbed. Placing the tap slightly

upstream of the convergence avoids the accelerating flow region where static pressure drops rapidly over a short distance.

The downstream tap (P2) is located 18.75 mm into the throat section, approximately halfway along its 32.5 mm length. This position was chosen to allow the flow to partially develop after entering the throat from the convergent section. Immediately after the convergent-throat transition, the velocity profile may be non-uniform due to boundary layer effects from the steep convergence angle. Placing the tap at the midpoint of the throat provides some axial distance for the flow to stabilize while remaining within the constant-diameter section where the static pressure measurement is most meaningful.

Both pressure taps are small holes perpendicular to the flow axis in the Venturi tube wall. Short lengths of 3D-printed piping connect these taps to the two prongs on the SDP810 differential pressure sensor.

4. Justification for no divergent section

A standard industrial Venturi tube as specified in ISO 5167-4 includes a divergent (diffuser) section downstream of the throat [51]. The purpose of the divergent section is to recover the kinetic energy of the high-velocity throat flow by gradually decelerating it back to near-inlet velocity, thereby minimizing the permanent pressure loss across the device [51]. This pressure recovery is important in piped industrial systems where the Venturi is installed in-line and the downstream piping requires adequate pressure to maintain flow.

In the present application, the exhaled air exits the Venturi throat directly to the atmosphere. Since there is no downstream piping to drive, the pressure recovery function is not required. While omitting the divergent section theoretically increases the permanent pressure loss (manifesting as slightly higher exhalation resistance), the low flow velocities involved make this increase negligible. The air simply expands into the ambient environment after passing through the throat. This elimination reduces the total length of the Venturi tube by approximately 50%, which is a significant advantage for a mask-mounted device where size and weight directly affect wearability.

The absence of the divergent section does mean that the Venturi geometry does not conform to any ISO 5167-4 standard geometry, so the tabulated C_d correlations from the standard are not applicable.

However, as discussed in Chapter II, the small scale and non-standard geometry of the tube already require empirical C_d determination. The aerodynamic effects of the sudden expansion are therefore absorbed into the overall empirical C_d value, which is determined through calibration with a reference flow standard as detailed in Chapter VI.

5. 3D printing and material considerations

All structural and mechanical components were 3D printed: the left compartment (electronics, battery, and perfboard housing), the central section (valve housing, honeycomb flow straightener, and CPAP cushion attachment mount), the right compartment (Venturi tube and sensor housing), and both one-way valves. All were fabricated using polyethylene terephthalate glycol (PETG) filament on a consumer-grade 3D printer (Bambulab X1 Carbon). PETG was selected over polylactic acid (PLA) for its superior moisture resistance, as the components are exposed to humid exhaled air during use. PETG also has better impact resistance and slightly higher temperature tolerance than PLA, reducing the risk of deformation during extended use [56].

The total filament consumption for all printed components was approximately 200 g. Standard print settings were used: a layer height of 0.2 mm with three perimeter walls and 20% infill. The Venturi tube was printed with the flow axis oriented horizontally to minimize the number of layer lines on the internal bore surface. Layer lines oriented perpendicular to the flow direction act as surface roughness elements that increase viscous losses and affect C_d. The dimensional tolerance of consumer grade 3D printers is typically $\pm$0.1 mm to $\pm$0.2 mm, which means the actual throat diameter may deviate slightly from the nominal 20 mm. Once C_d is determined empirically through calibration with a reference flow standard, these manufacturing imperfections will be inherently absorbed into the calibrated C_d value rather than requiring separate correction.

D. Electronic Component Selection and Circuit Design

As established earlier, computing VO_2 through indirect calorimetry requires three simultaneous measurements: volumetric airflow (from differential pressure across the Venturi tube), expired oxygen concentration, and expired carbon dioxide concentration. Each measurement is handled by a dedi-

cated sensor selected to balance cost, accuracy, and interface compatibility. Chapter II described the operating principles of the relevant sensor technologies; this section presents the specific components chosen, the rationale for each selection, and how they are interconnected. All three sensors communicate via I^2C, which simplifies the wiring to a shared two-wire bus.

1. Differential pressure sensor: Sensirion SDP810-500Pa

The Sensirion SDP810-500Pa is a digital differential pressure sensor based on a microelectromechanical systems thermal flow sensing element, as described in Chapter II [6]. Its key specifications for this application are a measurement range of $\pm$500 Pa, a resolution of 0.1 Pa, and a maximum sampling rate of approximately 2000 Hz (0.5 ms) in continuous measurement mode [6]. The sensor communicates over I^2C and provides factory-calibrated digital output, eliminating the need for external analog-to-digital conversion or complex user-side calibration routines [6].

The 500 Pa range was selected based on the pressure drop calculations in Section C: expected differential pressures range from approximately 5 Pa during moderate breathing to approximately 60 Pa during peak exercise flow rates, with occasional higher values possible during forced exhalation maneuvers. The 500 Pa range provides sufficient headroom for these peaks while the 0.1 Pa resolution ensures adequate sensitivity at the low end.

The 10 Hz sampling rate was established as a preliminary baseline to capture the temporal dynamics of respiratory flow. Given that a typical breath cycle lasts 1 to 3 seconds during exercise [38], a 10 Hz rate yields 10 to 30 samples per cycle, providing sufficient resolution for initial flow integration. This frequency represents a balance between temporal resolution and data transmission overhead; however, the sampling rate remains a tunable parameter in the system firmware. Future human subject testing will empirically evaluate whether increasing the sampling frequency yields statistically significant improvements in volume calculation accuracy.

2. Oxygen sensor: DFRobot Gravity electrochemical sensor

The DFRobot Gravity oxygen sensor (model SEN0322) is a galvanic electrochemical sensor with an onboard I^2C interface [7]. The sensor measures oxygen concentration over a range of 0 to 25% with a

Figure 9. The Sensirion SDP810-500Pa digital differential pressure sensor [6].

resolution of 0.15% and a specified response time (T_{90}) of $\leq$ 15 seconds [7]. While the electrochemical reaction rate limits the physical response speed, the onboard microcontroller continuously digitizes the sensor output. This allows the main system to poll the sensor at 0.5 Hz (every 2 seconds) to capture the transient response curve, simplifying integration with the ESP32 microcontroller.

The primary trade-off in selecting an electrochemical sensor is this response characteristic. As discussed in Chapter II, commercial metabolic carts use paramagnetic oxygen analyzers with sub-100-millisecond response times, enabling true breath-by-breath gas analysis [48]. The slower response of the electrochemical sensor acts as an intrinsic low-pass filter, meaning it cannot resolve the rapid intra-breath concentration changes. However, this hardware behavior physically mimics the integration of a mixing chamber. Consequently, the limitation is accommodated by the post-processing methodology described in Section F: rather than computing instantaneous gas exchange, the system treats the sensor output as a rolling average of expired oxygen concentration. The approximate cost of $54 is two to three orders of magnitude lower than a paramagnetic analyzer, making this trade-off acceptable for a low-cost screening tool.

3. Carbon dioxide sensor: Sensirion SCD30

The Sensirion SCD30 is a nondispersive infrared (NDIR) carbon dioxide sensor module that also provides integrated temperature and relative humidity (RH) measurements [8]. Its CO_2 measurement range spans 0 to 40,000 ppm (0 to 4%), with a specified accuracy of $\pm$30 ppm + 3% of the measured

Figure 10. The DFRobot Gravity electrochemical oxygen sensor (SEN0322) [7].

value within the 400 to 10,000 ppm calibrated range. Outside this range, accuracy is not guaranteed by the manufacturer. The measurement interval is 2 seconds, and the sensor communicates over I^2C or UART.

Expired CO_2 concentrations during exercise typically reach 4 to 5% (40,000 to 50,000 ppm) at maximal effort [38]. The sensor's 40,000 ppm upper limit covers the majority of the expected operating range. However, it is important to note that measurements between 10,000 and 40,000 ppm lie outside the factory calibration points and rely on sensor linearity, likely resulting in accuracy degradation beyond the specified 3%. Furthermore, concentrations at or near maximal exertion may approach or exceed this ceiling. In practice, the system operates primarily in the sub-maximal range where expired CO_2 remains well within the sensor's specified range, and the mixing-chamber averaging approach further mitigates the impact of brief excursions near the measurement limit. Similar to the oxygen sensor, the 2-second measurement interval is slower than the gas analyzers in commercial metabolic carts but is sufficient for the averaged post-processing approach used in this system.

The co-measurement of temperature and relative humidity is a practical advantage. Air density, which appears in the Venturi flow equation (Equation 2.5), depends on temperature and humidity. Exhaled air is typically near body temperature (approximately 37°C) and fully saturated with water vapor,

conditions that differ significantly from the ambient air used during calibration. The SCD30's temperature and humidity readings enable air density corrections during post-processing without requiring separate dedicated sensors, reducing component count and wiring complexity.

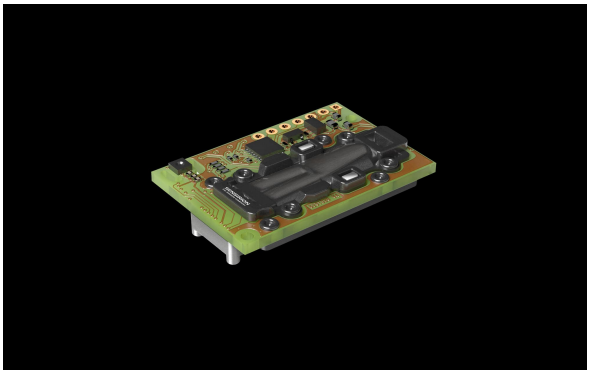

Figure 11. The Sensirion SCD30 nondispersive infrared carbon dioxide sensor module [8].

4. Microcontroller selection: ESP32 TTGO T-Display

The ESP32 TTGO T-Display V1.1 was selected as the central microcontroller for the system. The ESP32 system-on-chip provides built-in BLE and WiFi radios, a dual-core 240 MHz processor, and flexible general-purpose input/output pins, all at a cost of approximately $10 [57]. The TTGO T-Display variant adds a 1.14-inch color thin-film transistor display, a USB-C connector for programming and charging, and an integrated lithium polymer battery charging circuit with a JST connector for direct battery attachment. These integrated features reduce the number of external components needed: the display, although not entirely necessary, provides real-time feedback during operation and is convenient for quick verification and debugging, and the battery management circuit eliminates the need for a separate charging module. The ESP32's built-in Bluetooth Low Energy radio is essential for wireless data transmission to the logging laptop. Its I^2C peripheral supports the shared bus architecture used to communicate with all three sensors. The dual-core processor allows sensor polling and

BLE transmission to run concurrently without timing conflicts, which is important given the 10 Hz sampling rate of the pressure sensor.

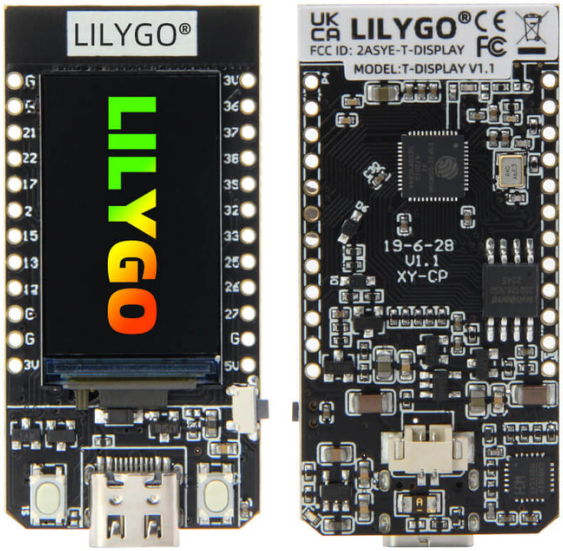

Figure 12. The LILYGO TTGO T-Display V1.1 ESP32 development board with integrated 1.14-inch LCD [9].

5. I2C bus architecture and Circuitry

All three sensors share a single I^2C bus. The bus is configured on GPIO 25 (SDA) and GPIO 26 (SCL) rather than the ESP32's default I^2C pins (GPIO 21 and GPIO 22), because the default pins were physically damaged on the development board during early prototyping. The ESP32's I^2C peripheral supports custom pin assignment through software configuration, so this reassignment required only a firmware change with no hardware modification.

Two 4.7 kΩ pull-up resistors connect the SDA and SCL lines to the 3.3 V supply rail, as required by the I^2C specification for proper signal integrity. Red and black wires carry power (3.3 V and ground),

while green and blue wires carry the SDA and SCL signals. These four wires are soldered directly to the microcontroller's GPIO pads and terminated in a 4-pin JST-XH connector.

This connector plugs into a custom 3D-printed holder that houses a small perfboard. The perfboard serves as a distribution hub: it receives the power and I^2C signals from the microcontroller, routes them through the pull-up resistors, and splits them into three male JST-XH connectors, one for each sensor. Each sensor has a matching female JST-XH connector on its cable, enabling tool-free connection and disconnection for ease of assembly and maintenance. This modular connector approach allows individual sensors to be replaced without resoldering.

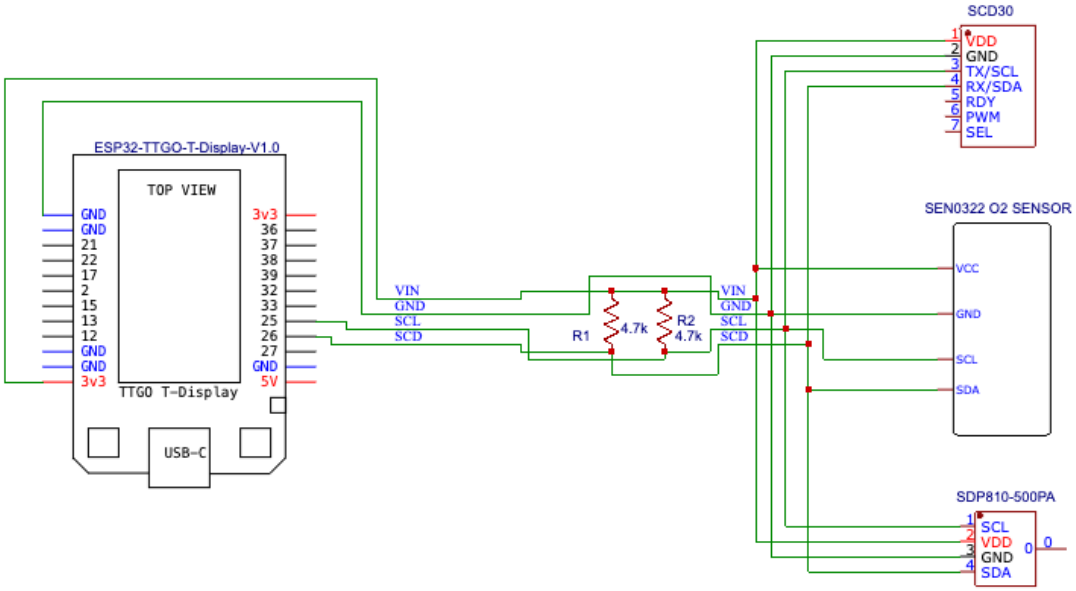

Figure 13. Schematic of the data acquisition circuit showing the ESP32 TTGO T-Display connected to the SCD30, SEN0322, and SDP810 sensors over a shared I^2C bus with 4.7 kΩ pull-up resistors.

Figure 14 shows the interior of the electronics housing (left compartment) with the ESP32 microcontroller and the slide-in perfboard with JST-XH connectors on both sides. Figure 15 shows the sensor compartment from above.

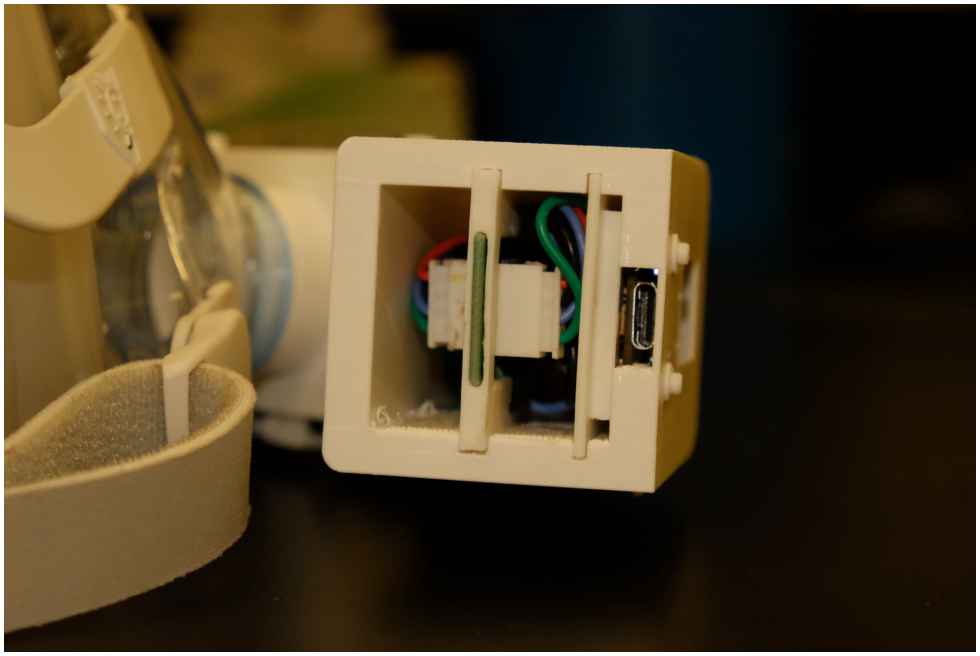

Figure 14. Interior of the electronics housing (left compartment) showing the ESP32 TTGO T-Display, the slide-in perfboard with JST-XH connectors on both sides, and the USB-C port for programming and battery charging.

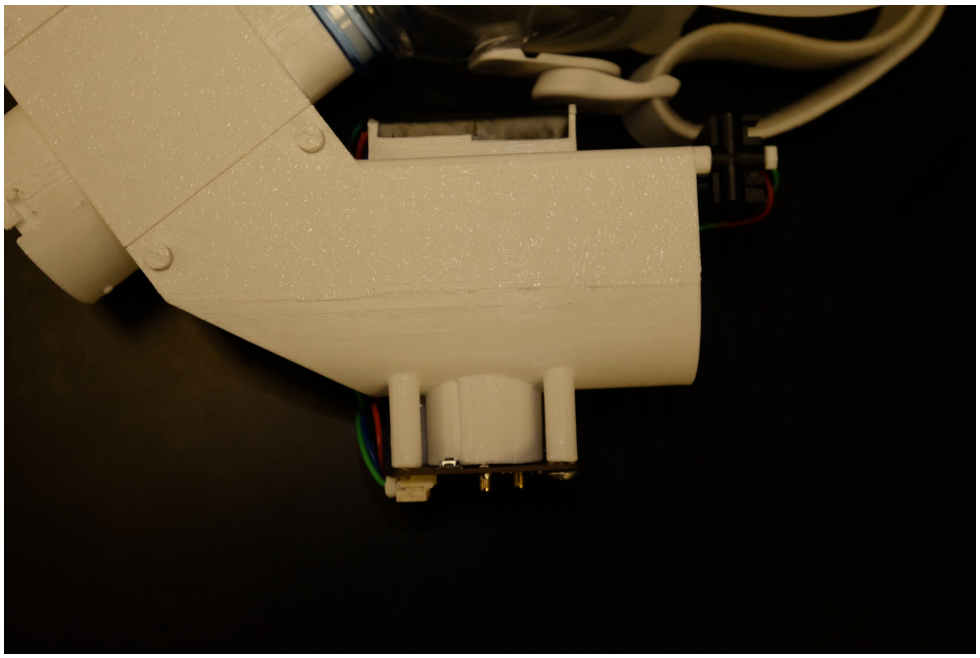

Figure 15. Sensor compartment (right compartment) viewed from the top. The Venturi tube is housed inside this section.

The wires connecting the electronics section (left side of the enclosure) to the sensor section (right side) run along the bottom of the entire assembly through designed cable management slots. This external routing keeps the wires out of the airflow path and prevents them from interfering with the one-way valves or the Venturi tube inside the enclosure.

E. Firmware Development

The firmware was developed in C++ using the Arduino framework in Visual Studio Code using the PlatformIO integrated development environment (IDE) extension. PlatformIO manages the ESP32's toolchain, library dependencies, and build configuration, which simplifies reproducibility: the complete build environment is defined in a single configuration file that can be version-controlled alongside the source code. The firmware is responsible for three tasks: polling the sensors over the I^2C bus, transmitting the data wirelessly over Bluetooth Low Energy, and displaying real-time readings on the built-in thin-film transistor screen.

1. I2C sensor communication

At startup, the firmware initializes the I^2C bus on the non-default pins described in Section D and performs a sequential initialization of each sensor. The SDP810 is configured for continuous measurement mode with temperature compensation and averaging. In this mode the sensor measures continuously at its maximum internal rate (up to approximately 2 kHz) and averages all samples acquired since the previous I^2C read, writing the result to its I^2C result buffer [6]. The firmware retrieves this averaged value every 100 ms (10 Hz), so each reading effectively integrates approximately 200 internal samples. The SCD30 is started with its minimum supported measurement interval of 2 seconds. The DFRobot oxygen sensor requires no explicit mode configuration and begins providing readings immediately after power-on.

The main loop polls the sensors at the rates established in Section D. The SDP810 is read every 100 ms (10 Hz), yielding one averaged differential pressure sample per cycle. The SCD30 and DFRobot oxygen sensor are read every 2 seconds (0.5 Hz); the firmware checks the SCD30's data-ready flag before reading, and the DFRobot sensor's electrochemical response time makes sub-second

polling unnecessary. Each oxygen reading is the average of 10 consecutive ADC samples taken within a single poll, which smooths electrical noise at the analog front end before the value enters the digital pipeline. Each sensor has a unique I^2C address, so all three coexist on the shared bus without address conflicts. If an I^2C read fails (indicated by a non-zero return code from the Wire library), the firmware silently substitutes a zero value and continues to the next polling cycle rather than halting, which prevents a single sensor glitch from disrupting the entire data stream.

2. Dual-rate BLE transmission protocol

A key firmware design decision was the implementation of a dual-rate Bluetooth Low Energy transmission protocol to accommodate the different sensor sampling rates. Two BLE characteristics are defined within a single BLE service. The "fast" characteristic carries the differential pressure reading and is updated at 10 Hz, matching the SDP810 polling rate. The "slow" characteristic carries the oxygen concentration, carbon dioxide concentration, temperature, and humidity readings and is updated at 0.5 Hz, matching the gas sensor polling rate.

This dual-rate approach was adopted because the pressure data requires high temporal resolution for accurate breath detection and flow integration, while the gas sensors cannot provide meaningful new data faster than approximately 0.5 Hz: the SCD30's minimum measurement interval is 2 seconds, and the electrochemical oxygen sensor's 15-second response time renders sub-second polling redundant. Transmitting all data at 10 Hz would either waste bandwidth by repeating stale gas sensor values or require the receiving software to distinguish fresh readings from repeated ones. Transmitting all data at 0.5 Hz would undersample the pressure signal and lose the temporal detail needed for breath cycle delineation. The dual-rate design cleanly separates the two data streams, and the receiving software merges them by timestamp as described in Section F.

Each BLE characteristic transmits its data as a packed binary struct using little-endian byte order. The fast characteristic sends an 8-byte packet containing a `uint32` timestamp in milliseconds followed by a 32-bit float for the differential pressure in pascals. The slow characteristic sends a 20-byte packet containing a `uint32` timestamp followed by four 32-bit floats: oxygen concentration in percent, carbon dioxide concentration in parts per million, temperature in degrees Celsius, and relative

humidity in percent. Binary packing minimizes packet size and avoids the overhead of string formatting and parsing. The BLE notification mechanism is used for both characteristics: the connected client receives each update automatically without needing to poll, which reduces latency and simplifies the client-side code.

(a) ESP32 firmware — packed BLE structs

```
struct __attribute__((packed)) FastPacket {
  uint32_t timestamp_ms;
  float  pressure_pa;
}; // 8 bytes, BLE notify at 10 Hz

struct __attribute__((packed)) SlowPacket {
  uint32_t timestamp_ms;
  float  o2_percent;
  float  co2_ppm;
  float  temperature_c;
  float  humidity_percent;
}; // 20 bytes, BLE notify at 0.5 Hz
```

(b) Python logger — binary unpacking and CSV columns

```
# Fast packet (8 bytes): little-endian uint32 + float
timestamp_ms, pressure_pa = struct.unpack("<If", data[:8])
# --> pressure CSV: timestamp, timestamp_ms, pressure_pa

# Slow packet (20 bytes): little-endian uint32 + 4 floats
timestamp_ms, o2, co2, temp, rh = struct.unpack("<Iffff", data[:20])
# --> slow CSV: timestamp, timestamp_ms, o2_percent,
#           co2_ppm, temperature_c, humidity_percent
```

Figure 16. BLE packet structures as defined in the firmware (a) and decoded by the Python logger (b). The `timestamp` column in each CSV is the laptop's reception time; `timestamp_ms` is the ESP32's `millis()` value embedded in the packet.

3. TFT display interface

The TTGO T-Display's built-in 1.14-inch color thin-film transistor screen displays real-time sensor readings during operation. The display shows the current differential pressure in pascals, oxygen concentration as a percentage, carbon dioxide concentration in parts per million, temperature in degrees Celsius, relative humidity as a percentage, and the SDP810's on-chip temperature. The SDP810 temperature is displayed for diagnostic purposes only and is not transmitted over BLE. The display updates at the slower 0.5 Hz rate to avoid excessive screen refresh overhead on the microcontroller.

The primary purpose of the display is operational verification: it allows the user to confirm that all sensors are functioning and returning reasonable values before beginning a measurement session. During early prototyping, the display was instrumental in diagnosing sensor communication failures and identifying wiring issues without requiring a laptop connection. While the display is not essential for data collection (all data is transmitted over BLE), it provides a useful confirmation that the system is operating correctly.

Figure 17 shows the display during active data collection, and Figure 18 shows the paused state indicating no BLE connection.

F. Data Logging and Analysis Software

The data logging and analysis pipeline is currently implemented in Python and runs on a laptop, where a single script handles raw data visualization, breath detection, flow rate calculation, and VO_2 computation. A post-processing approach was chosen over real-time computation to allow rapid iteration on the analysis algorithms and validation of each stage before deployment. Because BLE is the sole communication interface, any BLE-capable device—including a smartphone running a dedicated iOS or Android application—can replace the laptop. Once the algorithms are validated, the transition to live on-device computation requires changes only to the receiving application; the firmware and BLE protocol remain unchanged.

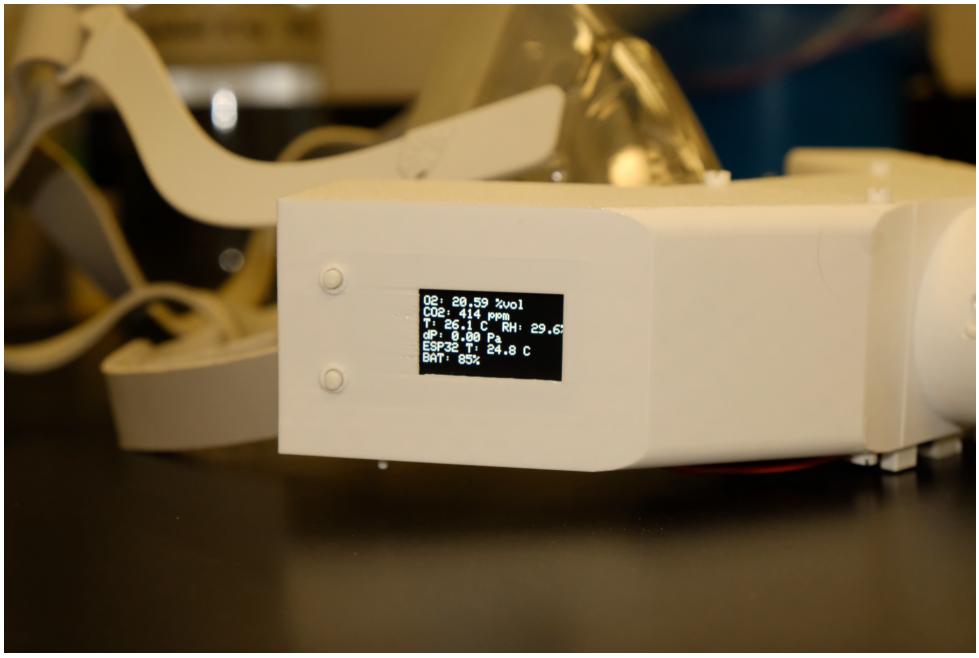

Figure 17. TFT display during active data collection showing real-time sensor readings

Figure 18. TFT display showing the paused state when no BLE client is connected. The display indicates the system is powered and operational but not actively transmitting data.

1. BLE data reception and stream merging

The Python logging script uses the Bleak library, an asynchronous Bluetooth Low Energy client, to connect to the ESP32 and receive data from both BLE characteristics. Bleak provides callback-based notification handling: when the ESP32 updates either the fast or slow characteristic, the corresponding callback function is invoked automatically with the new data.

Each incoming data packet carries the ESP32's `millis()` timestamp from the moment of sampling and is additionally timestamped using the laptop's system clock at the moment of reception; both values are recorded in the CSV output. The fast and slow streams are written to separate CSV files to preserve the native sampling rate of each stream without padding the slow channels with repeated values or leaving sparse columns in a single file. During post-processing, the two files are merged by timestamp and the slow sensor values are forward-filled between updates, so that each 10 Hz pressure sample is associated with the most recent gas sensor reading. Since the gas concentrations change slowly relative to the 2-second update interval, this forward-fill approach introduces negligible error compared to the inherent sensor response time limitations.

The analysis script also produces a raw data visualization: time-aligned plots of differential pressure, CO_2 concentration, and O_2 concentration on vertically stacked axes with summary statistics (mean, standard deviation, minimum, maximum, range, and sample count) for each channel. This plot serves as a quick quality check: it confirms that all sensors were active throughout the session, highlights any dropout periods, and provides an at-a-glance summary of the recorded data before reviewing the computed results.

2. Breath detection algorithm

Individual breath cycles are identified from the differential pressure waveform recorded by the SDP810 sensor. During exhalation, air flows through the Venturi tube from the mask toward the atmosphere, producing a positive pressure differential. During inhalation, air is drawn in through a separate one-way valve (described in Section G), and the pressure differential drops to near zero.

The breath detection algorithm scans the differential pressure signal for sign changes (zero-crossings). Each pair of consecutive zero-crossings defines a phase of either positive or negative pressure. The al-

gorithm discards all negative-pressure phases (which correspond to inhalation intervals or minor valve backflow) and evaluates only the positive-pressure phases as candidate exhalations. A candidate exhalation is accepted only if its peak pressure exceeds a minimum threshold of 0.5 Pa and its duration falls between 0.3 and 10 seconds; phases that fail either criterion are rejected as sensor noise or non-respiratory transients. Only the accepted exhalation phases, where air flows through the Venturi tube past the gas sensors, are used for flow integration and gas exchange computation.

3. Flow rate calculation

For each 10 Hz differential pressure sample during an exhalation phase, the instantaneous volumetric flow rate is computed using the Venturi equation (Equation 2.5 from Chapter II), restated here for reference:

$$Q = C_d \cdot A_2 \cdot \sqrt{\frac{2\Delta P}{\rho\,(1-\beta^4)}} \tag{3.5}$$

where all parameters are as defined in Section C. The discharge coefficient $C_d = 0.97$ is the literature-based estimate discussed in Section C; the air density ρ is set to a baseline value of 1.2 kg/m^3, with SCD30 temperature and humidity readings available for a corrected density calculation in future work. The exhaled volume for each breath is obtained by numerically integrating the flow rate over the exhalation duration using the trapezoidal rule over the recorded timestamps.

4. VO_2 computation methodology

The minute ventilation V_E is computed by summing the exhaled volumes of all breath cycles within a rolling 60-second window:

$$V_E = \sum_{\text{breaths}} \int_{\text{exhale}} Q\,dt \tag{3.6}$$

Because the system measures only expired gas flow through the Venturi tube, the inspired minute ventilation V_I must be derived using the Haldane transformation introduced in Chapter II (Equation 2.2):

$$V_I = V_E \times \frac{1 - F_e\mathrm{O}_2 - F_e\mathrm{CO}_2}{1 - F_i\mathrm{O}_2 - F_i\mathrm{CO}_2} \tag{3.7}$$

where $F_iO_2 = 0.2093$ and $F_iCO_2 = 0.0004$ are the known fractions in ambient inspired air, and F_eO_2 and F_eCO_2 are the measured fractions in expired air. The expired CO_2 fraction is obtained from the SCD30 sensor reading in ppm divided by 10^6.

Oxygen consumption is then computed as the difference between the volume of oxygen inspired and the volume expired:

$$\dot{V}O_2 = (V_I \times F_iO_2) - (V_E \times F_eO_2) \tag{3.8}$$

Similarly, carbon dioxide production is computed as:

$$\dot{V}CO_2 = (V_E \times F_eCO_2) - (V_I \times F_iCO_2) \tag{3.9}$$

These equations yield the oxygen consumed and carbon dioxide produced for a single breath, in liters. Summing the per-breath values over a rolling 60-second window and multiplying by 1000 converts to milliliters per minute, which is the conventional reporting unit. The respiratory exchange ratio is computed as:

$$\text{RER} = \frac{\dot{V}CO_2}{\dot{V}O_2} \tag{3.10}$$

which provides an indicator of metabolic substrate utilization and exercise intensity [38].

The expired gas fractions F_eO_2 and F_eCO_2 are averaged over each exhalation phase individually, and the Haldane transformation, VO_2, and VCO_2 are computed per breath. The per-breath VO_2 and VCO_2 volumes are then summed over a rolling 60-second window to produce minute-rate values. Because the electrochemical oxygen sensor's 15-second response time (discussed in Section D) cannot resolve concentration changes within individual breaths, the per-breath gas fractions effectively represent a running average, approximating a mixing-chamber approach.

The analysis script produces a second plot showing the computed results: instantaneous flow rate during exhalation, tidal volume per breath, rolling VO_2 in mL/min, and the respiratory exchange ratio, each with summary statistics. Because the discharge coefficient has not been empirically determined and no human subject testing has been conducted, these computed values serve as a demonstration that the analysis pipeline is functional and ready for use once calibration and IRB approval are obtained.

G. Physical Assembly

The three-compartment enclosure described in Section B attaches to the CPAP mask cushion via the 40 mm inlet port. The electronics compartment on the left is sealed from the airflow path; no respiratory air passes through it. The two one-way valves in the central and right compartments enforce unidirectional airflow: inhaled air enters through the central valve, while exhaled air flows rightward through the Venturi tube past the gas sensors and exits to the atmosphere. Each valve consists of a flexible silicone sheet mounted over a 3D-printed frame; the sheet deflects open under positive pressure in the intended flow direction and seats flat against the frame to block reverse flow. This design, inspired by the valve mechanism in [37], is simple to fabricate and replace. However, because the silicone sheet is not a rigid seal, a strong inhalation can momentarily pull a small amount of air backward through the exhale valve before the sheet re-seats, producing a brief negative pressure transient in the Venturi tube (Section 2.). Re-engineering the valve geometry or switching to a stiffer membrane material is identified as a future improvement in Chapter VI. This separation ensures that, under normal breathing, only expired air is measured, as required by the open-circuit indirect calorimetry methodology.

(a) Front view (b) Back view (c) Silicone sheet deflection

Figure 19. The 3D-printed one-way valve assembly. (a) Front view showing the spoke frame and central post. (b) Back view showing the silicone sheet seated against the frame. (c) A finger demonstrates how the flexible silicone sheet deflects under pressure to permit airflow in one direction.

The external cable routing and management slots described in Section D keep all sensor wiring outside the airflow path. The total system weight including the mask cushion, enclosure, all sensors, microcontroller, battery, and wiring is approximately 350 g.

Figure 20 shows the fully assembled system from the front, with the CPAP mask cushion connected to the three-compartment enclosure. Figure 21 shows the underside of the assembly, revealing the external cable routing through the management slots that carry the I^2C and power wires from the electronics housing to the sensor compartment.

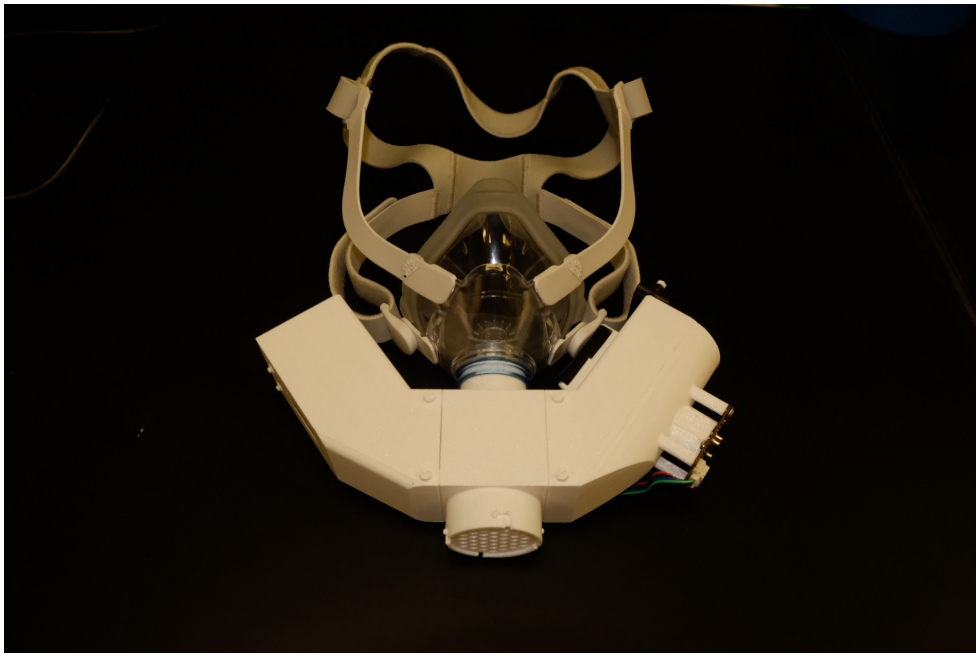

Figure 20. Fully assembled mask system viewed from the front. The CPAP cushion attaches to the central inlet port of the three-compartment 3D-printed enclosure. The electronics housing is on the left, the air intake port is at the front, and the sensor compartment is on the right.

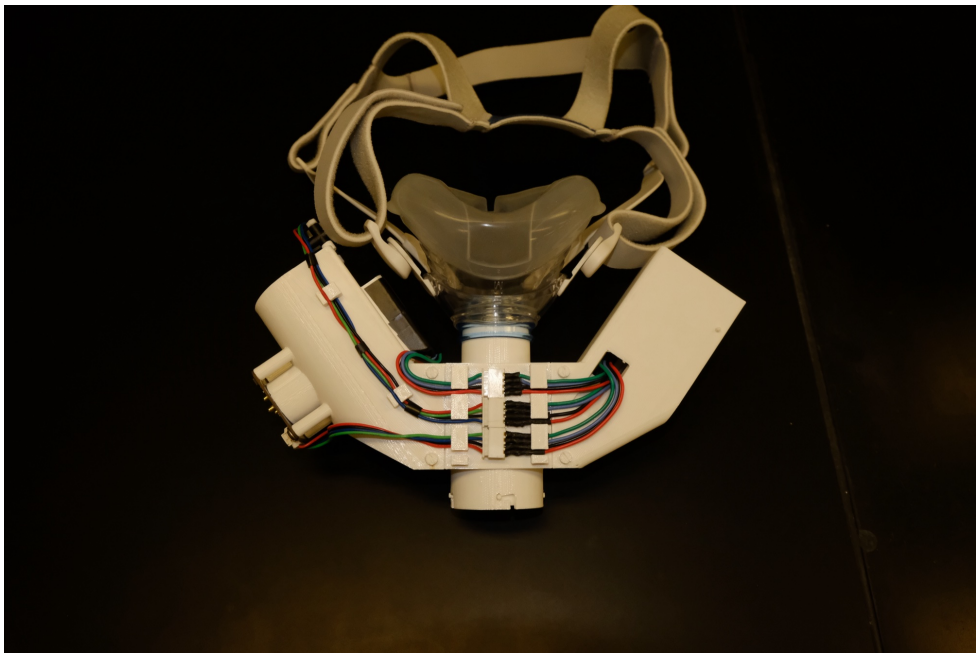

Figure 21. Underside of the assembled mask showing the external cable routing. The I^2C and power wires run through 3D-printed cable management clips along the bottom of the enclosure, keeping the wiring outside the airflow path.

CHAPTER IV.

SENSOR VERIFICATION AND CHARACTERIZATION

A. Overview of Verification Approach

All experiments presented in this chapter are instrument-level bench characterizations conducted without human subjects and without Institutional Review Board (IRB) approval. The objective is to confirm that each sensor functions correctly by comparing its response to known or expected stimuli under controlled conditions. These tests do not establish absolute quantitative accuracy; rather, they demonstrate functional readiness for the calibration and human-subject validation work described in Chapter VI.

No calibration syringe or reference spirometer was available for this work. Consequently, the differential pressure sensor is verified for zero-flow stability and qualitative airflow response, but the discharge coefficient C_d used in the flow computation (Chapter III, Section F) remains a literature-based estimate. Empirical determination of C_d is identified as the highest-priority item in the future work plan.

Three verification experiments were conducted:

1. **Ambient air baseline** (Section B): All sensors were logged simultaneously in open air to verify that readings match known atmospheric reference values.

2. **Controlled CO_2 generation** (Section C): An acid–base neutralization reaction was used to flood a sealed container with CO_2, simultaneously elevating CO_2 concentration and displacing O_2. This single experiment verifies both gas sensors.

3. **Differential pressure airflow response** (Section D): Brief controlled exhalations through the Venturi tube verified the pressure sensor's ability to resolve airflow-induced signals.

All three experiments used the complete data acquisition pipeline described in Chapter III: sensors polled via I^2C on the ESP32 microcontroller, transmitted wirelessly over BLE, received by the Python

logging client, and written to CSV files. Successful data collection in every experiment therefore implicitly verifies the full system integration, including firmware operation, BLE transmission reliability, timestamp synchronization between the 10 Hz and 0.5 Hz streams, and the data logging software.

B. Ambient Air Baseline Verification

Before performing stimulus-response tests, all three sensors were logged simultaneously in open air to establish that each sensor produces stable, physically plausible readings under known ambient conditions. The system was placed indoors in still air and powered on. Data were logged using the complete data acquisition pipeline for approximately 6 minutes (3,231 fast samples at 9.0 Hz, 180 slow samples at 0.5 Hz). Figure 22 shows the test setup during the ambient baseline phase, with the mask resting on top of the sealed container, the laptop displaying the terminal output, and a phone timer tracking the segment duration.

Figure 22. Ambient air baseline test setup. The mask assembly rests on the inverted container lid with the TFT display visible. The laptop screen shows the real-time BLE data stream in the terminal, and a phone timer tracks the 5-minute baseline duration.

The expected reference values at the test location are:

- **O_2:** 20.93%, the standard dry-air mole fraction [38].
- **CO_2:** approximately 420 ppm, consistent with the current global atmospheric average [8].
- **Differential pressure:** 0 Pa. With both Venturi ports open to the atmosphere and no airflow present, no pressure differential should exist. Any nonzero mean reading indicates a systematic offset, and the standard deviation quantifies the sensor noise floor under static conditions.

Table II summarizes the ambient baseline readings for all three sensors.

Table II. AMBIENT AIR BASELINE SENSOR READINGS

	Trial 1		Trial 2		
Sensor	Mean	Std Dev	Mean	Std Dev	Expected
O_2 (%)	20.53	0.04	20.50	0.04	20.93
CO_2 (ppm)	498	8.8	603	11.2	$\sim$420
ΔP (Pa)	0.002	0.012	-0.00	0.011	0.00

The O_2 sensor reported means of 20.53% (Trial 1) and 20.50% (Trial 2), approximately 0.40–0.43 percentage points below the expected 20.93% dry-air value. This systematic offset is consistent across both trials and likely reflects the sensor's factory calibration tolerance combined with the humidity at the test site, as the electrochemical cell measures partial pressure rather than mole fraction. The CO_2 sensor reported means of 498 ppm (Trial 1) and 603 ppm (Trial 2), both higher than the global average of approximately 420 ppm. These elevated readings are attributable to the indoor test environment, where human respiration and building ventilation typically produce CO_2 levels of 400–600 ppm; the higher Trial 2 baseline is consistent with reduced room ventilation between trials. The differential pressure sensor showed mean offsets of 0.002 Pa and -0.00 Pa with standard deviations of 0.012 Pa

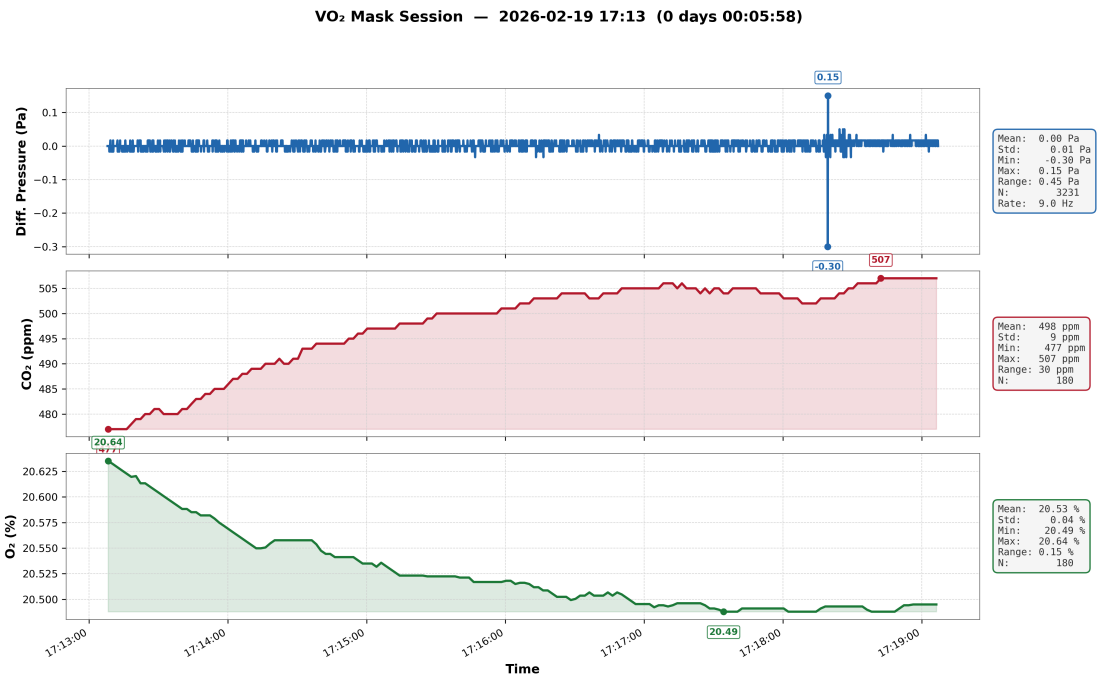

Figure 23. Ambient air baseline recording (Trial 1, 6 minutes). Top: differential pressure showing negligible offset. Middle: CO_2 concentration. Bottom: O_2 concentration.

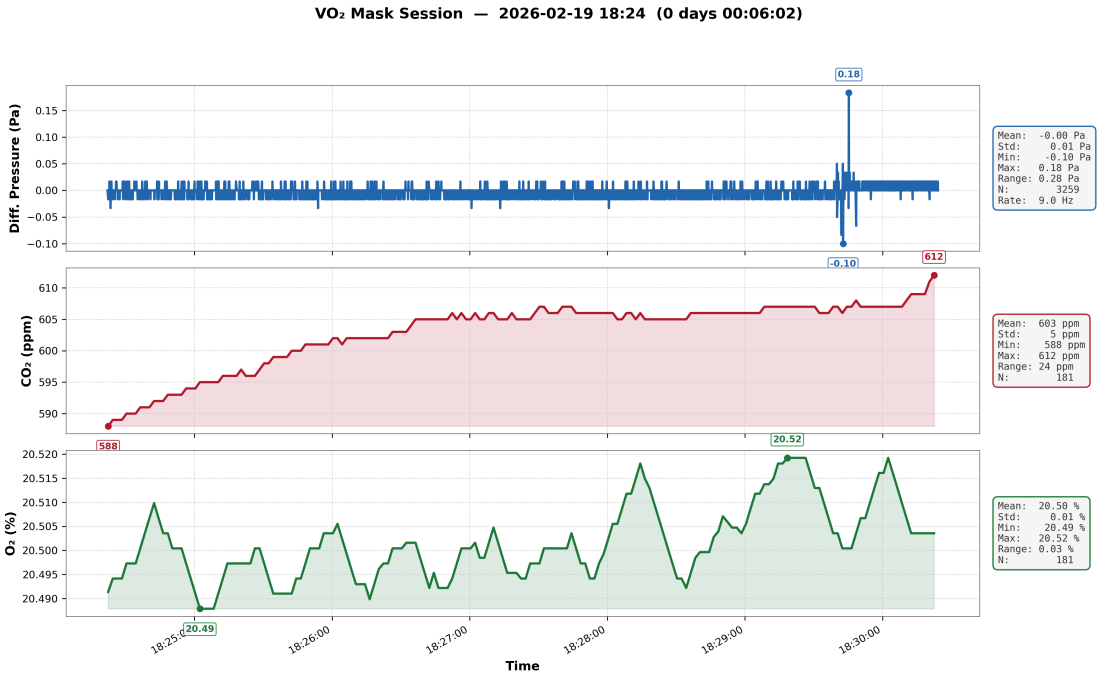

Figure 24. Ambient air baseline recording (Trial 2, 6 minutes). Top: differential pressure showing negligible offset. Middle: CO_2 concentration stable near 603 ppm. Bottom: O_2 concentration stable near 20.50%.

and 0.011 Pa, respectively, both negligible relative to the 0.5 Pa breath detection threshold used in the analysis pipeline.

A visible transient is present in the first minute of both baseline recordings: CO_2 begins below its steady-state value and rises, while O_2 starts slightly high and settles. This is an artifact of the test preparation: the sensor compartment was placed on top of an air purifier immediately before the recording began, flushing the sensor cavity with filtered, low-CO_2 air. The readings stabilize within approximately 60 seconds as the cavity equilibrates with the surrounding room air. The mean and standard deviation values in Table II are computed over the full recording and are therefore slightly influenced by this initial transient.

C. Gas Sensor Verification via Controlled CO_2 Generation

This section describes a combined verification test for both the CO_2 and O_2 sensors. A chemical reaction generates CO_2 inside a sealed container; the resulting increase in CO_2 concentration and simultaneous displacement of O_2 allow both gas sensors to be evaluated in a single experiment.

1. Chemistry of CO_2 production

Sodium bicarbonate (baking soda, $NaHCO_3$) reacts with acetic acid (CH_3COOH), the active component of household vinegar, in an acid–base neutralization that produces carbon dioxide gas, water, and sodium acetate [40]:

$$NaHCO_3 + CH_3COOH \rightarrow CH_3COONa + H_2O + CO_2\uparrow \tag{4.1}$$

The reaction proceeds rapidly at room temperature and produces a stoichiometrically determined quantity of CO_2, making it suitable for bench-level sensor verification without specialized laboratory equipment [40].

The reagents used were 100% sodium bicarbonate and commercially available white vinegar with a labeled acidity of 5% (i.e., 5 g of acetic acid per 100 mL of solution). Two 100 mL beakers were each loaded with 7 g of sodium bicarbonate and 80 mL of vinegar, yielding the following totals:

- Sodium bicarbonate: 14 g total (0.167 mol, $M_{NaHCO_3} = 84$ g/mol)

- Acetic acid: 8.0 g total from 160 mL of 5% vinegar (0.133 mol, $M_{\mathrm{CH_3COOH}} = 60.05$ g/mol)

The 1:1 stoichiometry of Equation 4.1 makes acetic acid the limiting reagent. The slight excess of sodium bicarbonate (0.167 mol vs. 0.133 mol) ensures complete reaction of the acid. The theoretical CO_2 yield is therefore 0.133 mol. Applying the ideal gas law at 25°C and 1 atm:

$$V_{\mathrm{CO_2}} = \frac{nRT}{P} = \frac{0.133 \times 8.314 \times 298}{101{,}325} \approx 3.3\ \mathrm{L} \tag{4.2}$$

2. Test apparatus

The test apparatus consisted of a rectangular polypropylene container with internal dimensions of 95 mm × 188 mm × 255 mm, yielding an internal volume of approximately 4.55 L. The mask assembly was placed inside the container with the circuitry facing upward in case the solution overflowed. Two beakers (100 mL capacity), each preloaded with 7 g of sodium bicarbonate, were placed alongside the mask. The effective free air volume inside the sealed container, after accounting for the mask assembly (≈0.27 L) and the beakers, was approximately 4.0 L.

The 3.3 L of CO_2 produced by the reaction is sufficient to displace approximately 80% of the original air in the container. This ensures that both sensors experience substantial concentration changes: the SCD30 CO_2 sensor is driven well beyond its 40,000 ppm (4%) measurement ceiling [8], while the O_2 concentration drops proportionally as CO_2 displaces the nitrogen–oxygen mixture.

3. Procedure

Each trial followed a three-phase protocol with the system logging continuously throughout all phases:

1. **Ambient baseline (5 minutes):** The mask was placed in open air. This established pre-stimulus reference readings for both gas sensors, consistent with the ambient values verified in Section B.

2. **Sealed container with CO_2 reaction (10 minutes):** 80 mL of vinegar was poured into each beaker containing sodium bicarbonate. The container lid was sealed immediately. The reaction produced vigorous effervescence lasting approximately 2–3 minutes, after which the CO_2 continued to diffuse and equilibrate throughout the container volume. Overflow of the fizzing liquid

Figure 25. Gas sensor verification test equipment. From left: laptop running the BLE logging script, box of sodium bicarbonate, bottle of 5% white vinegar, two 100 mL beakers, the polypropylene container with the mask assembly inside, and the container lid.

from the beakers was expected and posed no risk to the sensors, as the mask was oriented upside down slightly elevated from the bottom of the container.

3. **Recovery (∼40 minutes):** The container lid was opened, the mask was removed to open air, and logging continued until both sensors returned to near-baseline values.

Two trials were conducted to assess repeatability. Fresh reagents were prepared for each trial, and the container was ventilated between trials to ensure residual CO_2 did not affect subsequent baseline readings.

Figure 27 shows the sealed container during the CO_2 generation phase, with the reaction effervescence visible inside the beakers alongside the mask assembly. The laptop terminal output (Figure 28) shows the real-time BLE data stream during the sealed phase, with CO_2 at the 40,000 ppm sensor ceiling and O_2 declining as CO_2 displaces the air.

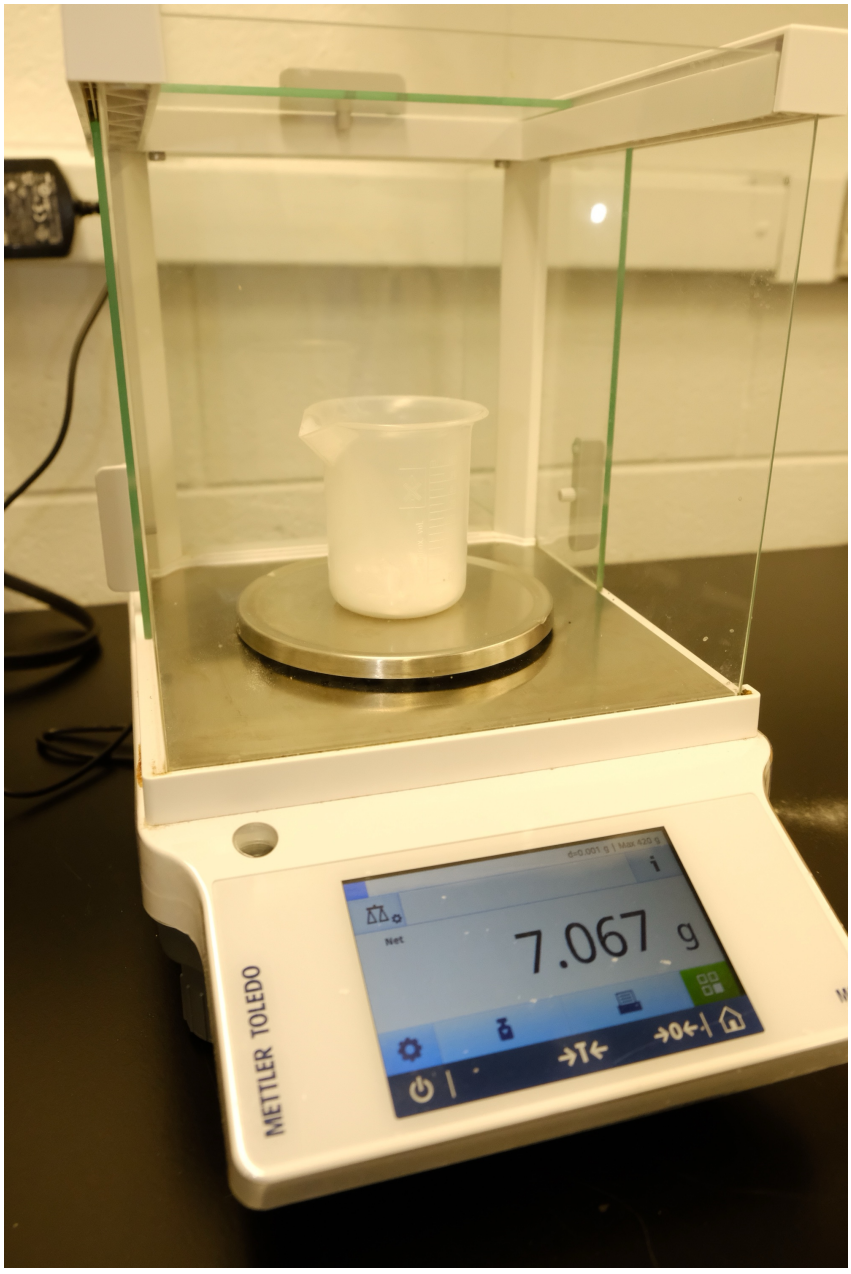

Figure 26. Sodium bicarbonate measured on an analytical balance, showing 7.067 g in a 100 mL beaker. Each trial used two such beakers for a total of 14 g of sodium bicarbonate.

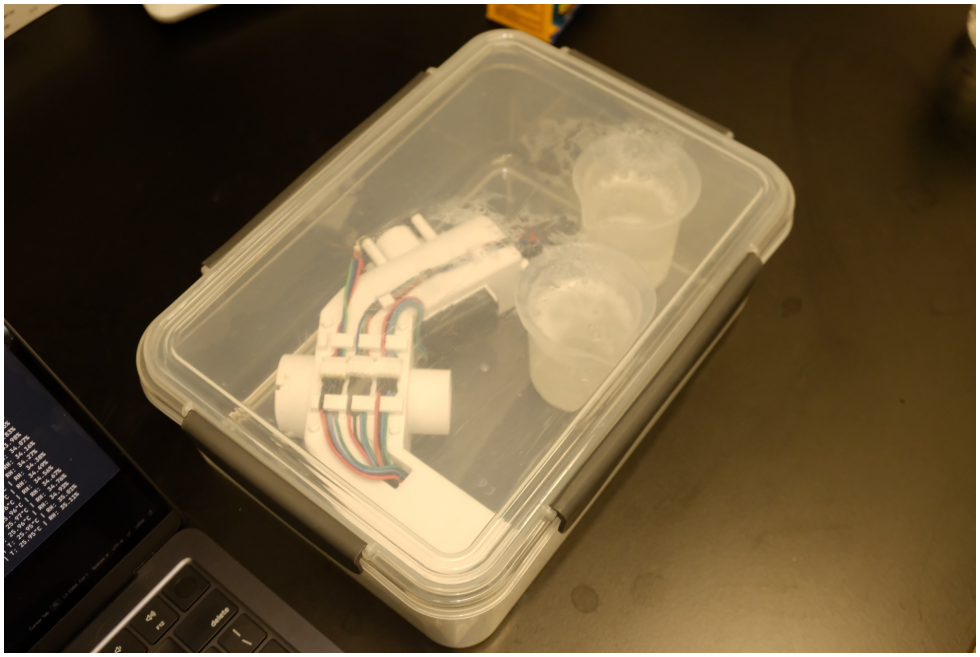

Figure 27. Sealed polypropylene container during the CO_2 generation phase. The mask assembly is visible on the left with the sensor compartment facing upward. The two beakers on the right contain the reacting sodium bicarbonate and vinegar mixture, with residual effervescence visible.

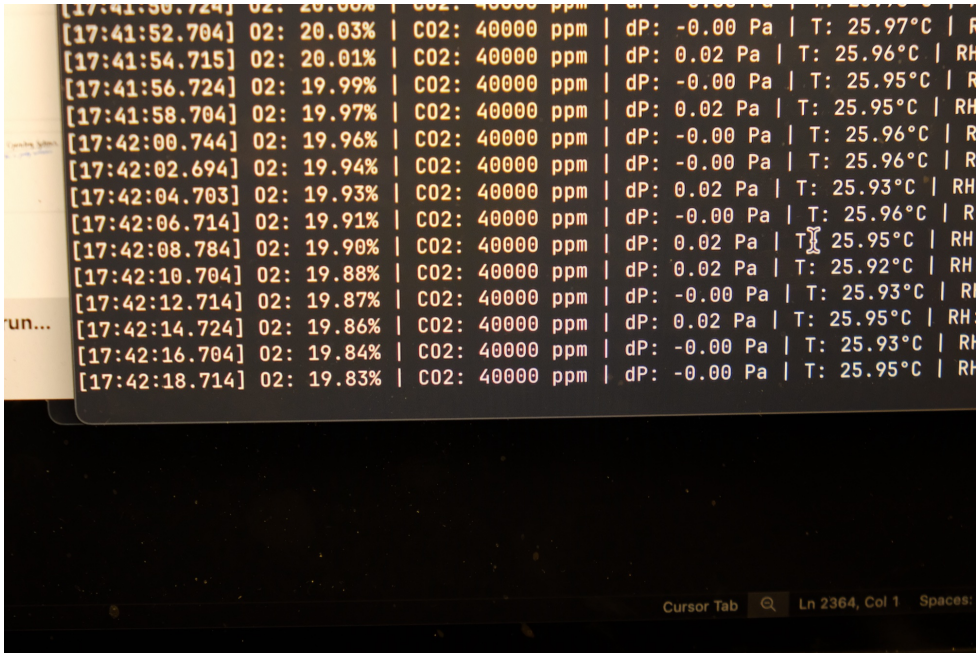

Figure 28. Close-up of the terminal output during the sealed container phase. Each line shows a timestamped reading with O_2 declining (19.83–20.03%), CO_2 saturated at 40,000 ppm, and differential pressure near 0 Pa.

4. Expected sensor response

CO_2 sensor (SCD30): The CO_2 concentration is expected to rise rapidly from the ambient baseline ($\sim$420 ppm) toward and beyond the sensor's 40,000 ppm measurement ceiling [8]. At the reagent quantities used, the equilibrium CO_2 concentration far exceeds this range; therefore, the sensor is expected to saturate at its maximum reading and remain there until the container is opened. During the recovery phase, the reading should decay back to ambient levels as CO_2 dissipates.

O_2 sensor (DFRobot SEN0322): As CO_2 fills the sealed container, it displaces the existing nitrogen–oxygen mixture. The O_2 concentration is expected to drop from $\sim$20.9% to a value determined by the remaining air fraction. The electrochemical sensor's slower response time ($T_{90} \leq 15$ s) [7] will produce a smoother transition curve compared to the CO_2 sensor's sharper rise. During recovery, O_2 should return to $\sim$20.9%.

The exact equilibrium concentrations inside the container depend on gas mixing dynamics, container seal quality, and CO_2 solubility in the reaction liquid. Therefore, this test does not establish absolute measurement accuracy for either sensor. Instead, it verifies four functional properties:

1. Both sensors respond to their target analyte in the correct direction.
2. The magnitude of response is physically plausible given the reagent quantities and container volume.
3. Both sensors recover to baseline values after the stimulus is removed.
4. The response pattern is repeatable across two trials.

5. Results

Figures 29–32 show the sensor responses during the sealed container and recovery phases for both trials. Table III summarizes the key metrics.

The CO_2 sensor responded rapidly upon sealing in both trials: the reading rose from its baseline to the sensor's 40,000 ppm measurement ceiling in 70 seconds (Trial 1) and 66 seconds (Trial 2), then remained saturated for the remainder of the sealed phase. This saturation is expected given that the

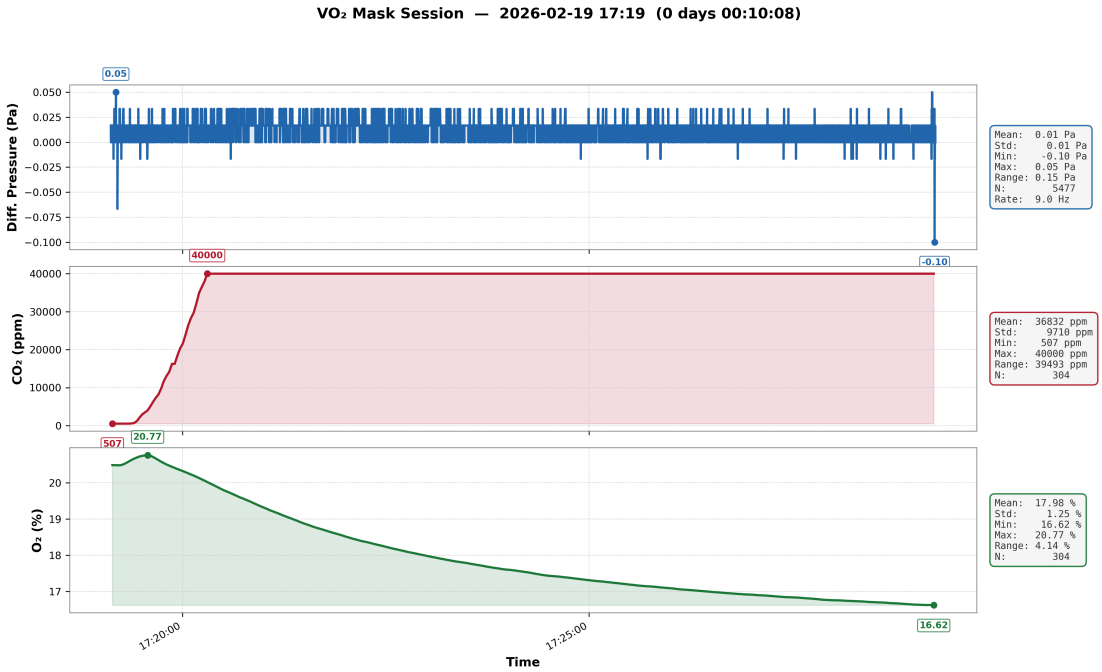

Figure 29. Sensor response during the sealed container phase of Trial 1 (10 minutes). CO_2 rises from 507 ppm to the sensor ceiling of 40,000 ppm within 70 seconds. O_2 drops from 20.49% to 16.62% over the full 10 minutes as CO_2 displaces the existing air. Differential pressure remains near zero, as expected in a sealed, static environment.

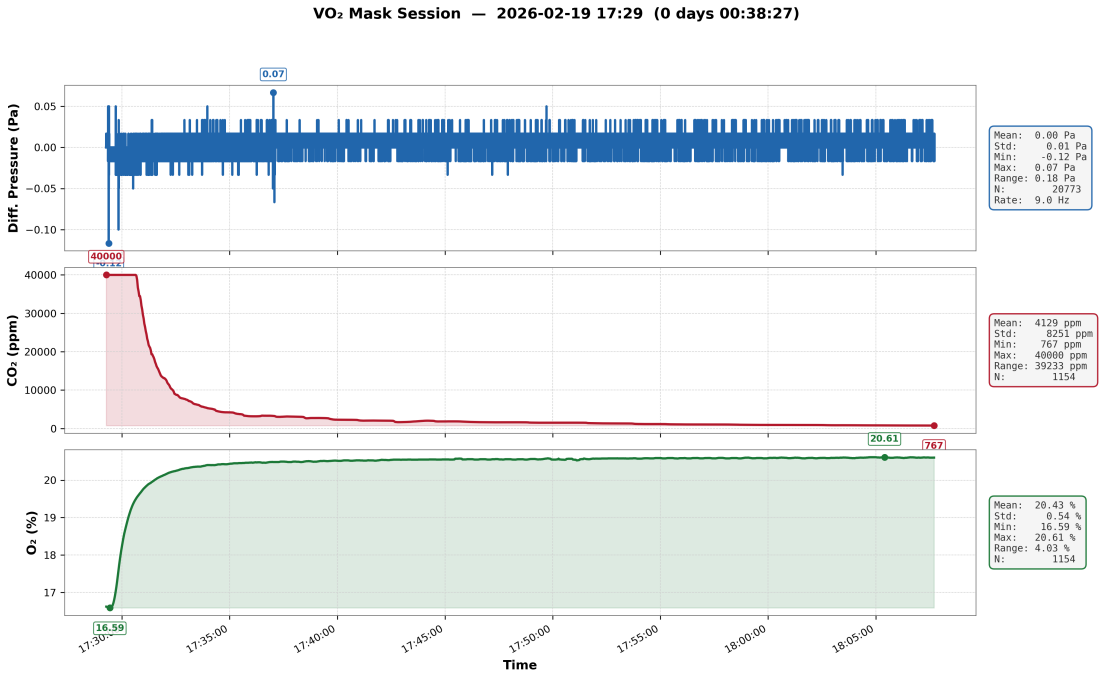

Figure 30. Recovery phase of Trial 1 (38 minutes). After the container lid was opened, CO_2 decayed from 40,000 ppm toward ambient levels, reaching 767 ppm by the end of the recording. O_2 recovered to within 0.5% of its baseline value within approximately 2 minutes and reached 20.60% by the end of the recording.

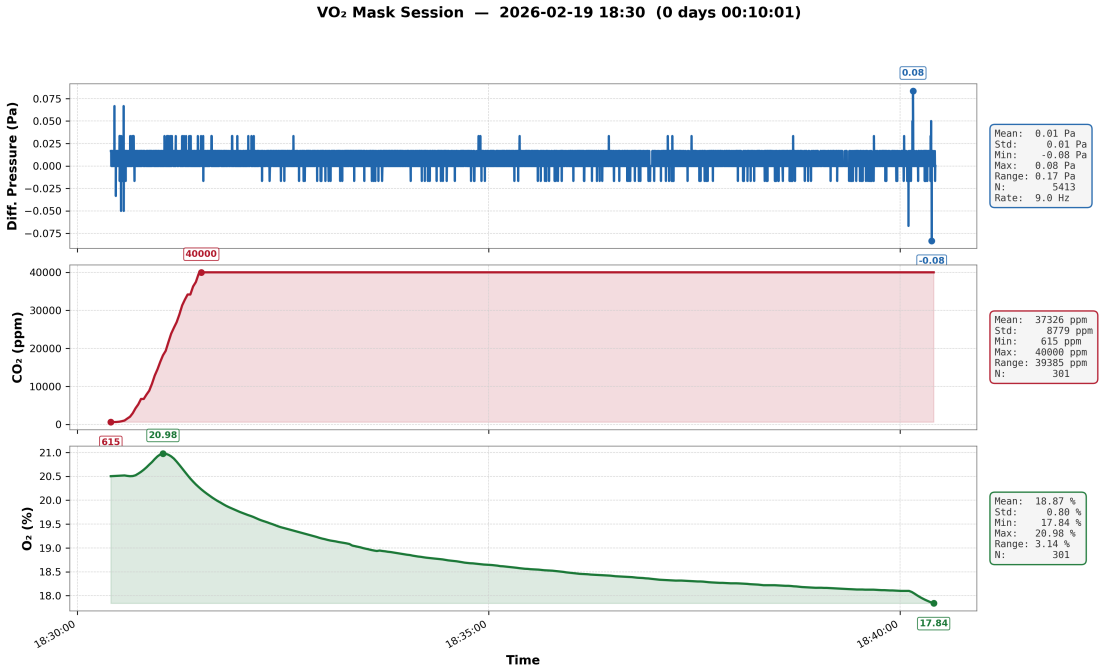

Figure 31. Sensor response during the sealed container phase of Trial 2 (10 minutes). CO_2 rises from 603 ppm to the sensor ceiling of 40,000 ppm within 66 seconds. O_2 drops from 20.50% to 17.84% over the full 10 minutes. The qualitative behavior matches Trial 1.

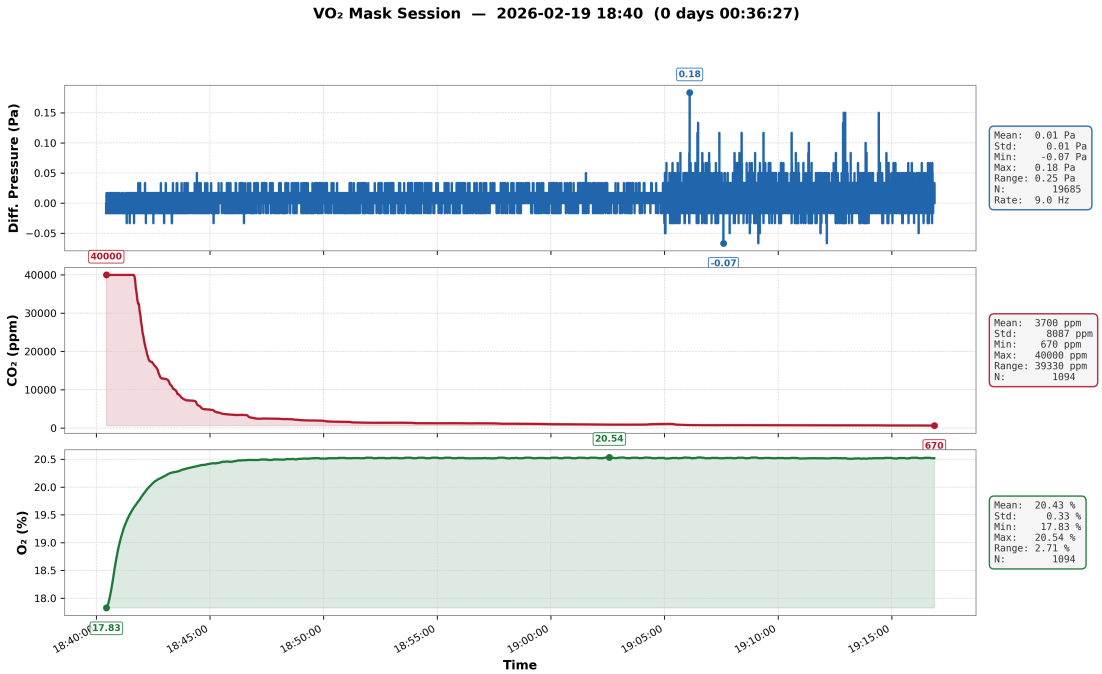

Figure 32. Recovery phase of Trial 2 (36 minutes). CO_2 decayed from 40,000 ppm to 670 ppm by the end of the recording. O_2 recovered to within 0.5% of its baseline value within approximately 2 minutes and reached 20.49% by the end of the recording.

Table III. GAS SENSOR RESPONSE SUMMARY

Parameter	Trial 1	Trial 2
CO_2 baseline (ppm)	498	603
CO_2 peak (ppm)	40,000	40,000
CO_2 time to peak (s)	70	66
CO_2 time to <1,000 ppm recovery (min)	29.3	20.5
CO_2 final reading (ppm)	767	670
O_2 baseline (%)	20.53	20.50
O_2 minimum (%)	16.62	17.84
O_2 time to minimum (min)	10.1	10.0
O_2 time to baseline $\pm$0.5% recovery (min)	2.3	1.9
O_2 final reading (%)	20.60	20.49

stoichiometric CO_2 yield (3.3 L) far exceeds the sensor's measurement range relative to the container volume. During recovery, the CO_2 concentration decayed with a long tail, requiring approximately 29 minutes (Trial 1) and 21 minutes (Trial 2) to drop below 1,000 ppm. The faster Trial 2 recovery is consistent with improved ventilation conditions during that trial. The slow decay reflects the time required for CO_2 trapped in the sensor housing and mask cavities to dissipate through passive diffusion.

The O_2 sensor showed a smooth, monotonic decline to minima of 16.62% (Trial 1) and 17.84% (Trial 2) over the 10-minute sealed phase. The 1.2 percentage point difference between trials likely reflects variability in the reaction vigor, container seal quality, and gas mixing dynamics. The gradual descent, in contrast to the CO_2 sensor's sharp rise, is consistent with the electrochemical sensor's 15-second T_{90} response time [7]. During recovery, O_2 returned to within 0.5% of its baseline value in approximately 2.3 minutes (Trial 1) and 1.9 minutes (Trial 2), substantially faster than the CO_2 recovery. This asymmetry is physically expected: O_2 recovery requires only that ambient air reach the sensor, whereas CO_2 recovery requires the dissipation of a high-concentration gas that continues to outgas from the reaction liquid.

Both trials demonstrate consistent qualitative behavior: rapid CO_2 saturation, monotonic O_2 displacement during the sealed phase, fast O_2 recovery followed by slow CO_2 decay. The quantitative differences between trials (time to CO_2 peak within 4 seconds, O_2 minima within 1.2 percentage

points) are within the range expected from an uncontrolled bench experiment with manually prepared reagents.

D. Differential Pressure Sensor Verification

The SDP810 differential pressure sensor was verified through two tests: a zero-flow stability measurement to characterize the sensor's noise floor and systematic offset, and a controlled airflow test to confirm the sensor resolves flow-induced pressure differentials through the Venturi tube.

1. Zero-flow stability

The ambient air baseline recording described in Section B provides the zero-flow stability data for the pressure sensor. With both Venturi ports open to the atmosphere and no airflow present, the differential pressure reading should be 0 Pa. The mean value of the recording quantifies any systematic offset, and the standard deviation characterizes the noise floor under static conditions. A low noise floor is essential for the breath detection algorithm (Chapter III, Section F), which uses a 0.5 Pa peak threshold to distinguish real exhalation events from sensor noise.

Table IV reports the zero-flow statistics extracted from the 6-minute ambient baseline recording (Section B).

Table IV. DIFFERENTIAL PRESSURE SENSOR ZERO-FLOW STATISTICS

Parameter	Value
Recording duration (min)	6.0
Mean offset (Pa)	0.002
Standard deviation (Pa)	0.012
Peak-to-peak range (Pa)	0.45

The mean offset of 0.002 Pa is negligible—less than 0.4% of the 0.5 Pa breath detection threshold. The standard deviation of 0.012 Pa indicates a noise floor more than 40 times smaller than the threshold, confirming that the sensor's static noise will not trigger false breath detections.

2. Controlled airflow response

To verify the sensor's ability to resolve airflow-induced pressure changes, the mask was worn in its normal operational configuration and a series of controlled breathing cycles were performed. Each cycle consisted of approximately 5 seconds of inhalation through the nose followed by approximately 3 seconds of steady exhalation through the mouth into the mask. The system logged continuously at 10 Hz throughout the 84-second recording (763 fast samples, 43 slow samples), during which 11 exhalation events were detected by the breath detection algorithm.

This test demonstrates three functional properties:

1. Exhalation produces a clear positive pressure deflection, and the signal returns to near zero between breaths, consistent with the one-way valve design in which no air should flow through the Venturi tube during inhalation. Small negative transients (~ -1.5 Pa) occasionally appear during forceful inhalation due to slight backflow through the flexible silicone valve (Chapter III, Section G). The return to baseline between cycles also confirms the absence of drift or hysteresis over short timescales.

2. The waveform pattern is repeatable across cycles, indicating consistent sensor behavior.

Because no calibration syringe or reference spirometer was available, this test cannot quantify volumetric flow rate accuracy. The discharge coefficient C_d used in the Venturi flow equation (Equation 2.5) remains a literature-based estimate of 0.97 [51]. Empirical C_d determination requires known reference flow rates and is addressed in the future work plan (Chapter VI).

Figure 33 shows the raw sensor data during the controlled breathing test. The differential pressure trace clearly resolves each exhalation cycle as a positive deflection (peak 2.65 Pa). Between exhalations the signal returns to near zero, as expected when the one-way valve blocks reverse flow through the Venturi tube. Occasional brief negative transients (minimum -1.48 Pa) appear during forceful in-

halation; these are attributed to slight backflow through the flexible silicone valve sheet before it fully re-seats, consistent with the valve characterization discussed in Chapter III, Section G. The transients are short-lived and the signal quickly returns to zero, confirming that the valve effectively separates the inhale and exhale pathways under normal breathing conditions.

The CO_2 trace oscillates between approximately 24,000 and 32,000 ppm, and the O_2 trace rises steadily from 14.65% to 18.32% over the 84-second recording. Prior to starting the deep breathing cycles, the mask was worn at rest with normal shallow breathing, during which O_2 gradually fell and CO_2 gradually rose in the sensor cavity. The transition to deep breathing reversed this trend. The gas sensor dynamics and their implications are discussed in Chapter V, Section A.

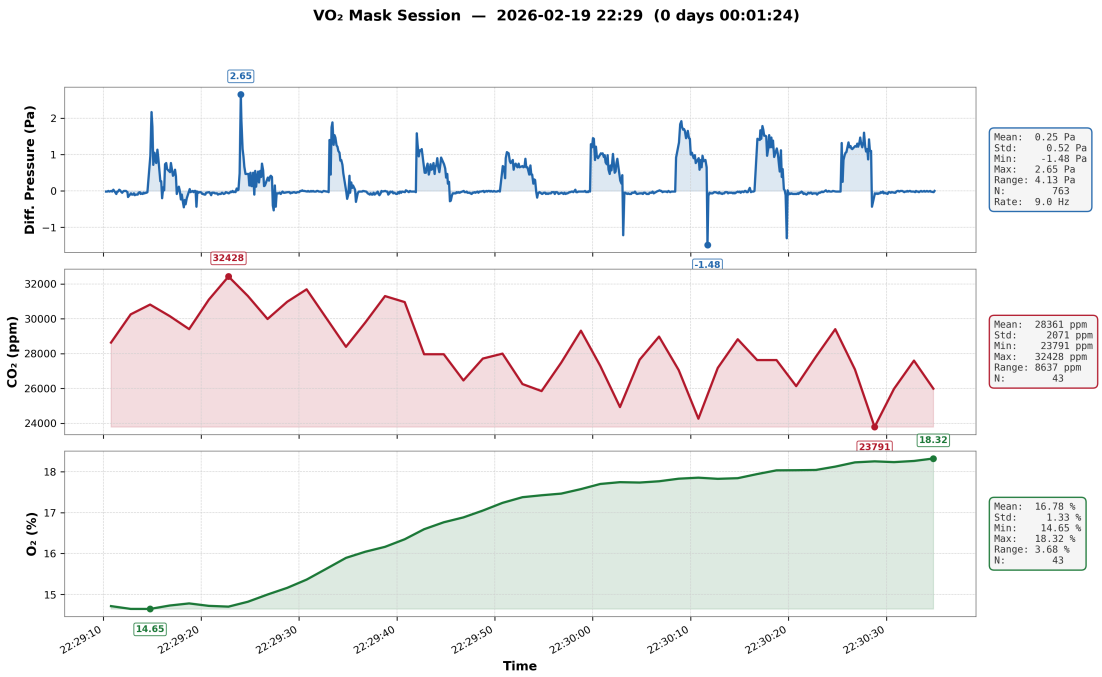

Figure 33. Raw sensor data during the controlled airflow response test (84 seconds, 11 detected breaths). Top: differential pressure showing repeatable exhalation peaks (positive) with the signal returning to near zero between breaths; occasional small negative transients reflect minor backflow through the silicone valve. Middle: CO_2 oscillating between ∼24,000 and 32,000 ppm. Bottom: O_2 rising from 14.65% to 18.32% as deep exhalations flush the sensor cavity with relatively O_2-rich expired air.

Figure 34 shows the computed analysis outputs. The flow rate trace resolves each exhalation event, with peak flow rates reaching 39.7 L/min and a mean of 21.9 L/min across detected exhalations. Tidal volume per breath ranged from 0.37 L to 1.35 L (mean 0.86 L), consistent with normal resting tidal volumes of 0.5–1.0 L. The increasing trend in tidal volume over the recording reflects the subject settling into a more consistent breathing pattern. The rolling VO_2 and respiratory exchange ratio (RER) are shown for completeness but are not physiologically meaningful for this bench test, as the subject was seated at rest and the gas sensor cavity had not yet reached steady-state concentrations (see Chapter V, Section A).

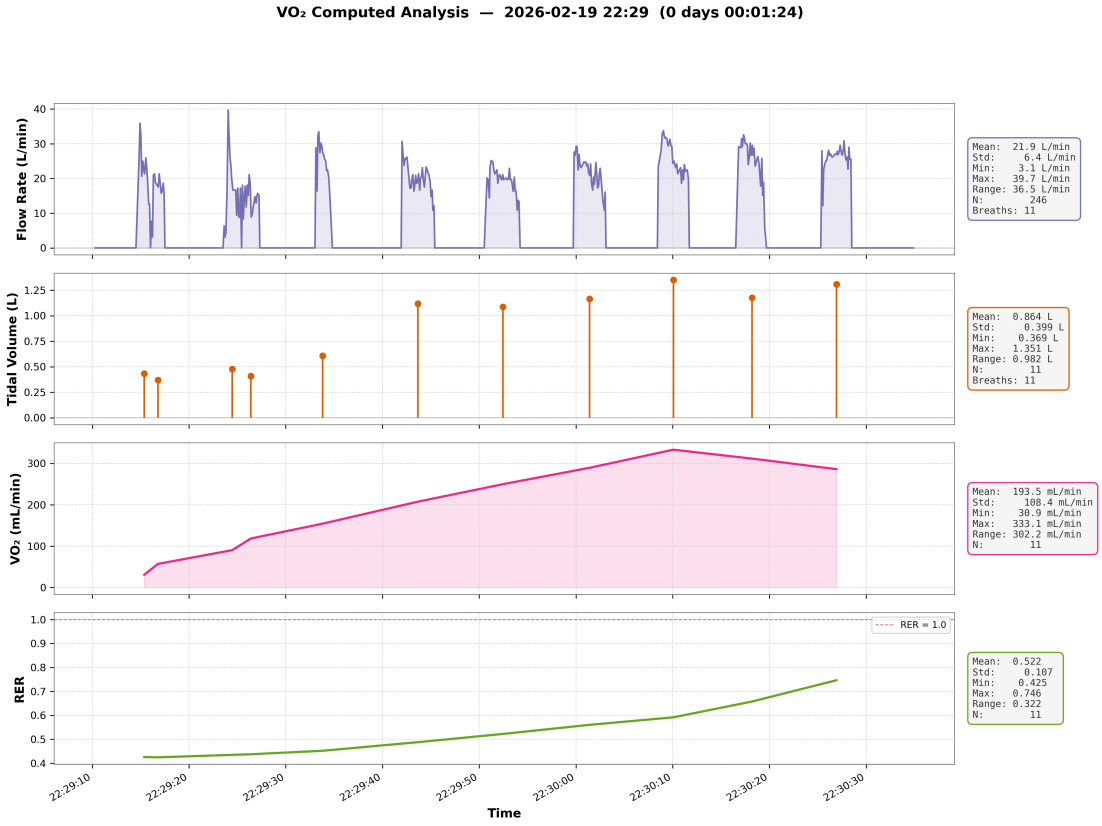

Figure 34. Computed analysis outputs for the controlled airflow test. Top: instantaneous flow rate during detected exhalations (mean 21.9 L/min, peak 39.7 L/min). Second: tidal volume per breath (mean 0.86 L). Third: rolling VO_2 (not physiologically valid for this bench test). Bottom: respiratory exchange ratio (RER).

CHAPTER V.

DISCUSSION

A. Interpretation of Sensor Dynamics

The verification experiments in Chapter IV established that all three sensors respond to their target stimuli in the expected direction and with physically plausible magnitudes. This section interprets what those responses mean for the intended metabolic cart application.

The CO_2 sensor's rapid saturation (Chapter IV, Section C) confirmed that it can reach 40,000 ppm in under 70 seconds. While the chemical test drove the sensor well beyond the physiological range of expired CO_2 (typically 35,000–50,000 ppm, or 3.5–5.0%), the implication for respiratory use is that the sensor can track the concentration difference between inspired and expired air within a single breath cycle, provided the respiratory rate remains below approximately 30 breaths/min. The 2-second measurement interval of the SCD30 is the practical limiting factor: at rest (12–20 breaths/min), each breath spans 3–5 seconds, allowing at least one CO_2 reading per breath. During heavy exercise at higher respiratory rates, the sensor may not resolve every individual breath, but the rolling 60-second averaging window used in the VO_2 computation pipeline (Chapter III, Section F) mitigates this limitation by accumulating multiple breath cycles.

The O_2 displacement and recovery curves (Chapter IV, Section C) reveal an important consequence of the electrochemical sensor's slow response time for respiratory gas analysis. The sensor cannot resolve the breath-by-breath oscillations in O_2 concentration that occur during respiration (typically 16–17% expired vs. 20.93% inspired). Instead, its output represents a running average of the gas mixture passing over it. As discussed in Chapter III, Section C, this hardware behavior effectively implements a mixing-chamber approach—commercial mixing-chamber systems use physically averaged gas samples, while this sensor achieves a similar averaging effect electrochemically. The absence of hysteresis during recovery (Chapter IV, Section C) further confirms that the sensor is suitable for repeated measurement sessions without requiring recalibration between tests.

The zero-flow stability results (Chapter IV, Section D) confirm that the breath detection threshold of 0.5 Pa provides a comfortable margin above the sensor noise floor. The more important open question is whether long-term drift over the duration of a typical exercise test (8–15 minutes) remains similarly small, given that temperature and humidity changes during exercise may affect the sensor. This has not yet been verified under exercise conditions.

The inherent lag between the fast pressure signal (10 Hz) and the slower gas concentration updates (0.5 Hz) confirms the necessity of the time-alignment and forward-fill strategy implemented in the data logging software (Chapter III, Section F). This lag is an intrinsic consequence of the dual-rate sampling architecture (Chapter III, Section E) and introduces negligible error given that the gas concentrations change slowly relative to the 2-second update interval.

The gas sensor behavior during the controlled airflow response test (Chapter IV, Section D) further illustrates the interaction between exhalation force, Venturi geometry, and sensor cavity flushing. The sensors sit in the exhale pathway downstream of the Venturi tube; the one-way intake valve prevents any airflow through the sensor cavity during inhalation. Before the deep breathing cycles began, the mask was worn at rest with normal shallow breathing. During this period, O_2 gradually fell and CO_2 gradually rose in the sensor cavity. This suggests that shallow resting exhalations do not generate sufficient flow through the Venturi constriction to fully flush the sensor cavity: small quantities of expired air seep past the sensors and mix with the stagnant cavity gas, causing CO_2 to slowly accumulate and O_2 to slowly deplete.

When deep breathing began (5-second inhalation, 3-second forceful exhalation), the increased expiratory force pushed substantially more air through the Venturi tube, effectively flushing the sensor cavity with each breath. At resting metabolic rates, the body extracts only a small fraction of the inhaled O_2, so expired air retains most of its oxygen content (typically 16–17%, compared to 20.93% in ambient air). These forceful exhalations therefore replaced the O_2-depleted stagnant gas with relatively O_2-rich expired air, producing the steady rise from 14.65% to 18.32% observed in Figure 33.

The CO_2 oscillations (24,000–32,000 ppm) reflect the pulsatile nature of exhalation. During each deep exhale, a bolus of expired air (approximately 4% CO_2, or 40,000 ppm at rest) flows past the sensor, driving the reading upward. Between breaths, no new air reaches the sensor; the stagnant

cavity gas diffuses and the CO_2 reading drifts downward. The SCD30's 2-second sampling interval captures this alternation as an oscillation whose amplitude depends on how many samples land during active exhalation versus during the inter-breath pause.

This observation has an important implication for the system's intended use during exercise: higher respiratory rates and greater tidal volumes during physical exertion will naturally produce more forceful and frequent exhalations, ensuring continuous flushing of the sensor cavity. The stagnation effect observed during shallow resting breathing is therefore unlikely to be a concern during actual VO_2 max testing, where ventilation rates are substantially elevated. The rolling 60-second averaging window used in the VO_2 computation pipeline would further smooth any residual oscillations into stable estimates.

B. Evaluation of System Constraints

A primary objective of this thesis was to demonstrate that a functional VO_2 max measurement system could be built at a fraction of the cost of commercial metabolic carts. The cost comparison presented in Chapter III (Table I) shows a bill of materials under $250, representing a cost reduction of over two orders of magnitude compared to cart-based systems. The key question is whether this cost reduction compromises measurement capability. The verification results in Chapter IV demonstrate that consumer-grade sensors are functionally capable of detecting the gas concentration changes and airflow patterns relevant to respiratory gas analysis, supporting the hypothesis that low-cost components can provide a viable alternative for non-clinical VO_2 max estimation. The remaining open question—whether this functional capability translates to quantitative accuracy—requires the calibration and validation work outlined in Chapter VI.

The 350 g system weight (Chapter III, Section G) is light enough to be supported by the CPAP mask harness without additional head-mounting hardware. For comparison, the COSMED K5 weighs approximately 900 g and requires a back-mounted harness with a sampling line to the face mask [3]. Unlike both cart-based systems and the K5, which require external tubing or sampling infrastructure, this system is entirely self-contained and mask-mounted. This portability enables use on indoor

treadmills and cycle ergometers as well as in field environments where cart-based systems cannot be deployed, such as outdoor running tracks, cycling courses, or athletic training facilities.

The modular three-compartment enclosure and JST-XH connector system described in Chapter III is a valuable design system. This modularity can potentially be used to facilitate future hardware upgrades, for example: substituting faster gas sensors without requiring a complete system redesign.

The verification experiments (Chapter IV) collectively demonstrate that all three measurement channels cover the dynamic ranges relevant to exercise testing. The remaining question is whether the sensor accuracies within those ranges are sufficient for clinically meaningful VO_2 max estimation, which requires the calibration work outlined in Chapter VI.

C. Reliability of Verification Methods

The verification experiments described in Chapter IV used proxy stimuli rather than the gold-standard calibration instruments typically employed in metabolic cart validation. This section evaluates what the chosen methods can and cannot establish about the system's measurement capabilities.

The acid–base neutralization test confirmed four functional properties (Chapter IV, Section C), but its uncontrolled variables (gas mixing dynamics, container seal quality, CO_2 solubility) prevent the equilibrium concentrations from serving as reference values. Notably, the CO_2 sensor saturated at its 40,000 ppm ceiling, so its accuracy at the physiologically relevant range of 30,000–50,000 ppm was not directly tested. Establishing absolute gas concentration accuracy would require calibration against certified reference gas mixtures, which was beyond the scope of this work.

The controlled airflow test (Chapter IV, Section D) was similarly limited to qualitative verification. Without a calibration syringe or reference spirometer, the discharge coefficient C_d remains the single largest source of uncertainty in any flow rate or VO_2 calculation produced by the system.

Despite these limitations, the verification methods establish that the system is functionally ready for the next validation step. All sensors respond correctly, the data acquisition pipeline operates reliably through the full chain from sensor polling to CSV output, and the system integration is confirmed by the successful collection of time-synchronized multi-sensor data across multiple trials. The path from this functionally verified prototype to a calibrated measurement instrument requires two steps:

empirical C_d determination using a calibration syringe, followed by human subject validation against a reference metabolic cart with IRB approval.

CHAPTER VI.

CONCLUSION

A. Challenges and Limitations

1. Interdisciplinary learning curve

This project was carried out by a single developer whose primary background was in software systems. Building a functional VO_2 max mask required acquiring working proficiency in several disciplines outside that background: embedded firmware design, analog and digital circuit construction, soldering technique, and mechanical CAD modeling. Each of these areas presented its own learning curve, and progress was often gated by domain knowledge that had to be acquired on the fly.

An illustrative example occurred during early circuit prototyping. The I^2C sensors would disconnect from the bus at random intervals despite being wired according to their datasheets. After extensive debugging, the root cause was identified as the absence of pull-up resistors on the I^2C clock and data lines—a standard requirement for open-drain buses that was not immediately obvious to someone without prior hardware experience. Adding 4.7 kΩ pull-up resistors resolved the issue entirely.

The scarcity of prior work in this space compounded the learning curve. The Instructables project [37] that inspired several component choices (Chapter III, Section B) was the closest available reference, but its design had practical limitations: a snorkel-inspired mouthpiece that required the user to block their nose and hold the device with one hand, and on-microcontroller VO_2 computation that limited analysis complexity. The system presented in this thesis addresses these shortcomings with a hands-free CPAP mask interface, separated airflow pathways, and a host-side computation pipeline (Chapter III, Section F).

Access to fabrication tools was essential and would have been a significant barrier without institutional support. Dr. Hampton-Marcell provided a 3D printer, filament, and circuitry tools through his laboratory, without which iterating on the mechanical design and circuit prototyping would have been far more difficult.

Only after developing a working understanding of Venturi tube physics, the datasheets and limitations of each sensor, embedded firmware design, mechanical CAD, and data analysis software was the complete system able to come together into the functional prototype described in this thesis.

2. Technical limitations

Several technical limitations constrain the current prototype:

1. **No empirical discharge coefficient.** As discussed in Chapter V, Section C, the literature-based C_d estimate is the single largest source of uncertainty in any flow rate or VO_2 calculation produced by the system.

2. **3D printing dimensional tolerances.** The $\pm$0.1–0.2 mm tolerance of consumer FDM printers (Chapter III, Section C) means the actual throat area may deviate from the nominal design. Without empirical calibration, this deviation remains an unquantified error source.

3. **Sensor response times.** The gas sensors' limited temporal resolution (Chapter III, Section D) prevents true breath-by-breath analysis. The mixing-chamber averaging approach is a practical workaround, but faster sensors would enable higher-fidelity measurements.

4. **One-way valve seal.** The silicone valve sheets allow slight backflow during forceful inhalation (Chapter IV, Section D). While the breath detection algorithm correctly rejects these transients, a re-engineered valve would improve airflow separation.

5. **No human subject validation.** All testing presented in this thesis is bench-level instrument characterization. The system has not been validated against a reference metabolic cart during actual exercise. IRB approval is required before human testing can proceed.

6. **Single prototype.** Only one unit was built and tested. Manufacturing repeatability across multiple units is unknown.

7. **Environmental sensitivity.** The effect of exercise-induced temperature, humidity, and body heat on sensor accuracy has not been characterized; all bench tests were conducted under stable indoor conditions.

8. **BLE reliability during exercise.** Packet loss during high-intensity exercise—where subject movement, sweat, and body positioning may degrade the wireless link—has not been characterized.

B. System Readiness Assessment

As concluded in Chapter V, Section C, the verification experiments establish the current prototype as a *functionally verified* system: all three sensors respond correctly, the full data acquisition pipeline operates reliably, and the VO_2 computation chain executes end-to-end. However, the system is not yet a *validated measurement instrument*. Two steps remain—empirical C_d calibration and human subject validation against a reference metabolic cart—before it can produce trusted VO_2 values. These steps are detailed in the following section.

C. Future Work

The following priorities are listed in the order they should be pursued, as each builds on the results of the preceding step.

1. Empirical Venturi discharge coefficient determination

The highest-priority next step is to determine the empirical discharge coefficient C_d of the 3D-printed Venturi tube by connecting it in series with a calibration syringe or reference spirometer and sweeping known flow rates across the respiratory range (approximately 20–200 L/min). Deriving C_d as a function of Reynolds number would convert the current flow computation from an estimate into a calibrated measurement.

2. IRB approval and human subject validation

After C_d calibration, the next step is to submit an IRB protocol for human subject exercise testing. The validation study would compare the system's VO_2 output against a commercial metabolic cart (the gold standard) during graded exercise tests on multiple subjects spanning a range of fitness levels. Agreement between the two systems would be assessed using Bland-Altman analysis to quantify systematic bias and limits of agreement [18].

3. Mobile application for real-time use

The current data pipeline requires a laptop running the Python logging client. For practical field use, a mobile application (iOS or Android) that receives BLE data directly on a smartphone would replace the laptop dependency. The application would port the validated analysis algorithms to on-device real-time computation, providing live VO_2 and RER display during exercise. The existing BLE protocol and firmware require no changes—only the receiver application is new. This step should follow human subject validation so that the algorithms being ported have been verified to produce accurate results.

4. Hardware improvements

Several hardware improvements would enhance the system's measurement capability and usability:

- **Faster gas sensors.** Substituting MEMS-based or optical O_2 sensors with sub-second response times would enable true breath-by-breath gas analysis, removing the reliance on the mixing-chamber averaging approach.
- **Custom PCB.** Replacing the perfboard prototype with a custom printed circuit board would improve connection reliability, reduce size, and simplify manufacturing for multiple units.
- **One-way valve re-engineering.** Redesigning the valve geometry or switching to a stiffer membrane material would reduce the backflow transients observed during forceful inhalation (Chapter IV, Section D).
- **Smoother Venturi bore.** Exploring resin printing or post-processing techniques (e.g., vapor smoothing) for the Venturi tube would reduce surface roughness from FDM layer lines, potentially improving the consistency of C_d across printed units.
- **Mask comfort and fit.** Optimizing the headband design, CPAP cushion selection, and weight distribution would improve comfort during extended exercise tests.

CITED LITERATURE

[1] COSMED, "Quark CPET: Cardiopulmonary exercise testing system," COSMED, 2024, available at: https://www.cosmed.com/en/products/cardio-pulmonary-exercise-test/quark-cpet. [Online]. Available: https://www.cosmed.com/en/products/cardio-pulmonary-exercise-test/quark-cpet

[2] ParvoMedics, "TrueOne 2400 metabolic measurement system," ParvoMedics, 2024, available at: https://www.parvo.com/trueone-2400/. [Online]. Available: https://www.parvo.com/trueone-2400/

[3] COSMED, "K5 wearable metabolic system: Technical specifications," COSMED, 2024, available at: https://www.cosmed.com/en/products/cardio-pulmonary-exercise-test/k5. [Online]. Available: https://www.cosmed.com/en/products/cardio-pulmonary-exercise-test/k5

[4] VO2 Master Health Sensors, "Vo2 master analyzer: Technical specifications and pricing," 2026, available at: https://vo2master.com/product/analyzer/. [Online]. Available: https://vo2master.com/product/analyzer/

[5] Wyatt Engineering, "The venturi effect," Wyatt Engineering, LLC, Lincoln, RI, 2024, available at: https://wyattflow.com. [Online]. Available: https://wyattflow.com

[6] Sensirion AG, *SDP810-500Pa Datasheet: Digital Differential Pressure Sensor*, Sensirion AG, Stäfa, Switzerland, 2023.

[7] DFRobot, *Gravity: I2C Oxygen Sensor (SEN0322) Wiki*, DFRobot, 2023, available at: https://wiki.dfrobot.com/Gravity_I2C_Oxygen_Sensor_SKU_SEN0322. [Online]. Available: https://wiki.dfrobot.com/Gravity_I2C_Oxygen_Sensor_SKU_SEN0322

[8] Sensirion AG, *SCD30 Datasheet: Sensor Module for HVAC and Indoor Air Quality Applications*, Sensirion AG, Stäfa, Switzerland, 2023.

[9] LILYGO, *TTGO T-Display ESP32 Development Board with 1.14 Inch LCD*, Shenzhen Xin Yuan Electronic Technology Co., Ltd., Shenzhen, China, 2024, available at: https://www.lilygo.cc/products/lilygo-ttgo-t-display-v1-1-esp32. [Online]. Available: https://www.lilygo.cc/products/lilygo-ttgo-t-display-v1-1-esp32

[10] D. R. Bassett and E. T. Howley, "Limiting factors for maximum oxygen uptake and determinants of endurance performance," *Medicine and Science in Sports and Exercise*, vol. 32, no. 1, pp. 70–84, 2000.

[11] A. V. Hill and H. Lupton, "Muscular exercise, lactic acid, and the supply and utilization of oxygen," *Quarterly Journal of Medicine*, vol. 16, no. 62, pp. 135–171, 1923.

[12] A. M. Jones and D. C. Poole, *Oxygen Uptake Kinetics in Sport, Exercise and Medicine*. London: Routledge, 2005.

[13] S. Kodama, K. Saito, S. Tanaka, M. Maki, Y. Yachi, M. Asumi, A. Sugawara, K. Totsuka, H. Shimano, Y. Ohashi, N. Yamada, and H. Sone, "Cardiorespiratory fitness as a quantitative predictor of all-cause mortality and cardiovascular events in healthy men and women: a meta-analysis," *JAMA*, vol. 301, no. 19, pp. 2024–2035, 2009.

[14] K. Mandsager, S. Harb, P. Cremer, D. Phelan, S. E. Nissen, and W. Jaber, "Association of cardiorespiratory fitness with long-term mortality among adults undergoing exercise treadmill testing," *JAMA Network Open*, vol. 1, no. 6, p. e183605, 2018.

[15] R. Ross, S. N. Blair, R. Arena, T. S. Church, J.-P. Després, B. A. Franklin, W. L. Haskell, L. A. Kaminsky, B. D. Levine, C. J. Lavie, J. Myers, J. Niebauer, R. Sallis, S. S. Sawada, X. Sui, and U. Wisløff, "Importance of assessing cardiorespiratory fitness in clinical practice: a case for fitness as a clinical vital sign," *Circulation*, vol. 134, no. 24, pp. e653–e699, 2016.

[16] American College of Sports Medicine, *ACSM's Guidelines for Exercise Testing and Prescription*, 11th ed. Philadelphia: Wolters Kluwer, 2021.

[17] M. J. Joyner and E. F. Coyle, "Endurance exercise performance: the physiology of champions," *Journal of Physiology*, vol. 586, no. 1, pp. 35–44, 2008.

[18] G. J. Balady, R. Arena, K. Sietsema, J. Myers, L. Coke, G. F. Fletcher, D. Forman, B. Franklin, M. Guazzi, M. Gulati, S. J. Keteyian, C. J. Lavie, R. Macko, D. Mancini, and R. V. Milani, "Clinician's guide to cardiopulmonary exercise testing in adults: a scientific statement from the American Heart Association," *Circulation*, vol. 122, no. 2, pp. 191–225, 2010.

[19] M. Cadena-Méndez, B. Escalante-Ramírez, J. Azpiroz-Leehan, and O. Infante-Vázquez, "VO_2 and VCO_2 variabilities through indirect calorimetry instrumentation," *SpringerPlus*, vol. 2, no. 1, p. 688, 2013.

[20] S. Priem, J. Jonckheer, E. De Waele, and J. Stiens, "Indirect calorimetry in spontaneously breathing, mechanically ventilated and extracorporeally oxygenated patients: An engineering review," *Sensors*, vol. 23, no. 8, p. 4143, 2023.

[21] D. J. Macfarlane, "Automated metabolic gas analysis systems: a review," *Sports Medicine*, vol. 31, no. 12, pp. 841–861, 2001.

[22] D. C. Nieman, M. D. Austin, D. Dew, and A. C. Utter, "Validity of COSMED's Quark CPET mixing chamber system in evaluating energy metabolism during aerobic exercise in healthy male adults," *Research in Sports Medicine*, vol. 21, no. 2, pp. 136–145, 2013.

[23] A. L. Woods, L. A. Garvican-Lewis, A. J. Rice, and K. G. Thompson, "The ventilation-corrected ParvoMedics TrueOne 2400 provides a valid and reliable assessment of resting metabolic rate in athletes compared with the Douglas bag method," *International Journal of Sport Nutrition and Exercise Metabolism*, vol. 26, no. 5, pp. 454–463, 2016.

[24] S. E. Crouter, A. Antczak, J. R. Hudak, D. M. DellaValle, and J. D. Haas, "Accuracy and reliability of the ParvoMedics TrueOne 2400 and MedGraphics VO2000 metabolic systems," *European Journal of Applied Physiology*, vol. 98, no. 2, pp. 139–151, 2006.

[25] L. D. Hodges, D. A. Brodie, and P. D. Bromley, "Validity and reliability of selected commercially available metabolic analyzer systems," *Scandinavian Journal of Medicine & Science in Sports*, vol. 15, no. 2, pp. 125–131, 2005.

[26] A. H. K. Montoye, J. D. Vondrasek, and J. B. Hancock, "Validity and reliability of the VO_2 Master Pro for oxygen consumption and ventilation assessment," *International Journal of Exercise Science*, vol. 13, no. 4, pp. 1382–1401, 2020.

[27] UCSF Human Performance Center, "Performance evaluations and pricing," University of California, San Francisco, 2024, available at: https://hpc.ucsf.edu/performance-evaluations. [Online]. Available: https://hpc.ucsf.edu/performance-evaluations

[28] UIC Campus Recreation, "Fitness testing services and pricing," University of Illinois Chicago, 2026, available at: https://recreation.uic.edu/fitness-wellness/fitwell-center/fitness-testing/. [Online]. Available: https://recreation.uic.edu/fitness-wellness/fitwell-center/fitness-testing/

[29] K. H. Cooper, "A means of assessing maximal oxygen intake: correlation between field and treadmill testing," *JAMA*, vol. 203, no. 3, pp. 201–204, 1968.

[30] L. A. Léger, D. Mercier, C. Gadoury, and J. Lambert, "The multistage 20 metre shuttle run test for aerobic fitness," *Journal of Sports Sciences*, vol. 6, no. 2, pp. 93–101, 1988.

[31] P.-O. Åstrand and I. Ryhming, "A nomogram for calculation of aerobic capacity (physical fitness) from pulse rate during submaximal work," *Journal of Applied Physiology*, vol. 7, no. 2, pp. 218–221, 1954.

[32] V. Noonan and E. Dean, "Submaximal exercise testing: clinical application and interpretation," *Physical Therapy*, vol. 80, no. 8, pp. 782–807, 2000.

[33] R.-J. Shei, I. G. Holder, A. S. Oumsang, B. A. Paris, and H. L. Paris, "Wearable activity trackers–advanced technology or advanced marketing?" *European Journal of Applied Physiology*, vol. 122, no. 9, pp. 1975–1990, 2022.

[34] P. Molina-Garcia, H. L. Notbohm, M. Schumann, R. Argent, M. Hetherington-Rauth, J. Stang, W. Bloch, S. Cheng, U. Ekelund, L. B. Sardinha, B. Caulfield, J. C. Brønd, A. Grøntved, and F. B. Ortega, "Validity of estimating the maximal oxygen consumption by consumer wearables: A systematic review with meta-analysis and expert statement of the INTERLIVE network," *Sports Medicine*, vol. 52, no. 7, pp. 1577–1597, 2022.

[35] S. E. Crouter, S. R. LaMunion, P. R. Hibbing, A. S. Kaplan, and D. R. Bassett, Jr., "Accuracy of the COSMED K5 portable calorimeter," *PLOS ONE*, vol. 14, no. 12, p. e0226290, 2019.

[36] I. Perez-Suarez, M. Martin-Rincon, J. J. Gonzalez-Henriquez, C. Fezzardi, S. Perez-Regalado, V. Galvan-Alvarez, J. W. Juan-Habib, D. Morales-Alamo, and J. A. L. Calbet, "Accuracy and precision of the COSMED K5 portable analyser," *Frontiers in Physiology*, vol. 9, p. 1764, 2018.

[37] Instructables Community, "DIY VO2 max measurement system," Online, 2020, accessed: 2025-01-15.

[38] K. Wasserman, J. E. Hansen, D. Y. Sue, W. W. Stringer, K. E. Sietsema, X.-G. Sun, and B. J. Whipp, *Principles of Exercise Testing and Interpretation: Including Pathophysiology and Clinical Applications*, 5th ed. Philadelphia: Lippincott Williams & Wilkins, 2012.

[39] M. F. Nunes, H. Plácido da Silva, L. Raposo, and F. Rodrigues, "Design and evaluation of a novel Venturi-based spirometer for home respiratory monitoring," *Sensors*, vol. 24, no. 17, p. 5622, 2024.

[40] S. S. Zumdahl, S. A. Zumdahl, and D. J. DeCoste, *Chemistry*, 10th ed. Boston: Cengage Learning, 2018.

[41] C. J. Gore, S. A. Clark, and P. U. Saunders, "Automated metabolic gas analysis systems: how much confidence can we have in them?" *International Journal of Sports Physiology and Performance*, vol. 8, no. 5, pp. 493–507, 2013.

[42] M. R. Miller, J. Hankinson, V. Brusasco, F. Burgos, R. Casaburi, A. Coates, R. Crapo, P. Enright, C. P. M. van der Grinten, P. Gustafsson, R. Jensen, D. C. Johnson, N. MacIntyre, R. McKay, D. Navajas, O. F. Pedersen, R. Pellegrino, G. Viegi, and J. Wanger, "Standardisation of spirometry," *European Respiratory Journal*, vol. 26, no. 2, pp. 319–338, 2005.

[43] A. Fick, "Über die Messung des Blutquantums in den Herzventrikeln," *Sitzungsberichte der Physikalisch-Medizinischen Gesellschaft zu Würzburg*, vol. 2, pp. XVI–XVII, 1870.

[44] J. R. Gifford, C. Blackmon, K. Hales, L. J. Hinkle, and S. Richards, "Overdot and overline annotation must be understood to accurately interpret $\dot{V}o_{2max}$ physiology with the fick formula," *Frontiers in Physiology*, vol. 15, p. 1359119, 2024.

[45] B. Saltin and J. A. L. Calbet, "Point: In health and in a normoxic environment, $\dot{V}\mathrm{O}_2$ max is limited primarily by cardiac output and locomotor muscle blood flow," *Journal of Applied Physiology*, vol. 100, no. 2, pp. 744–748, 2006.

[46] H. L. Taylor, E. Buskirk, and A. Henschel, "Maximal oxygen intake as an objective measure of cardio-respiratory performance," *Journal of Applied Physiology*, vol. 8, no. 1, pp. 73–80, 1955.

[47] C. G. Douglas, "A method for determining the total respiratory exchange in man," *Journal of Physiology*, vol. 42, no. Suppl, pp. xvii–xviii, 1911.

[48] S. A. Ward, "Open-circuit respirometry: real-time, laboratory-based systems," *European Journal of Applied Physiology*, vol. 118, no. 5, pp. 875–898, 2018.

[49] T. Meyer, T. Georg, C. Becker, and W. Kindermann, "Reliability of gas exchange measurements from two different spiroergometry systems," *International Journal of Sports Medicine*, vol. 22, no. 8, pp. 593–597, 2001.

[50] F. M. White, *Fluid Mechanics*, 8th ed. New York: McGraw-Hill Education, 2016.

[51] International Organization for Standardization, *Measurement of fluid flow by means of pressure differential devices inserted in circular cross-section conduits running full — Part 4: Venturi tubes*, International Organization for Standardization Std. ISO 5167-4:2003, 2003.

[52] P. Sridevi, P. Kundu, T. Islam, C. Shahnaz, and S. A. Fattah, "A low-cost Venturi tube spirometer for the diagnosis of COPD," in *TENCON 2018 — 2018 IEEE Region 10 Conference*, Jeju, Korea, 2018, pp. 723–726.

[53] K. Jasek, M. Pasternak, and M. Grabka, "Paramagnetic sensors for the determination of oxygen concentration in gas mixtures," *ACS Sensors*, vol. 7, no. 11, pp. 3228–3242, 2022.

[54] Joint Committee for Guides in Metrology, *Evaluation of Measurement Data — Guide to the Expression of Uncertainty in Measurement*, Bureau International des Poids et Mesures Std. JCGM 100:2008, 2008.

[55] M. Reader-Harris, W. Brunton, J. Gibson, and D. Hodges, "Discharge coefficients of venturi tubes with non-standard convergent angles," in *Proceedings of the 10th International Conference on Flow Measurement (FLOMEKO 2000)*. Salvador, Brazil: IMEKO, June 2000.

[56] M.-H. Hsueh, C.-J. Lai, S.-H. Wang, Y.-S. Zeng, C.-H. Hsieh, C.-Y. Pan, and W.-C. Huang, "Effect of printing parameters on the thermal and mechanical properties of 3d-printed pla and petg, using fused deposition modeling," *Polymers*, vol. 13, no. 11, p. 1758, 2021.

[57] Espressif Systems, *ESP32 Series Datasheet*, Espressif Systems, Shanghai, China, 2024, available at: https://www.espressif.com/sites/default/files/documentation/esp32_datasheet_en.pdf. [Online]. Available: https://www.espressif.com/sites/default/files/documentation/esp32_datasheet_en.pdf

VITA

NAME: Shashwat Sinha

EDUCATION: B.S., Computer Engineering, University of Illinois Chicago, Chicago, Illinois, 2024

M.S., Electrical and Computer Engineering, University of Illinois Chicago, Chicago, Illinois, 2026

PROFESSIONAL EXPERIENCE: Hardware Engineering Intern, Apple Inc., Cupertino, California, 2025

Graduate Research Assistant, Marcell Lab, University of Illinois at Chicago, Chicago, Illinois, 2024–2026